ELSEVIER

Contents lists available at ScienceDirect

Results in Optics

journal homepage: www.sciencedirect.com/journal/results-in-optics



Low-power all-optical photonic crystal synapse using Ge₂Sb₂Te₅ phase-change material

Amir Hossein Abdollahi Nohoji, Parviz Keshavarzi, Mohammad Danaie * 💿

Faculty of Electrical and Computer Engineering, Semnan University, Semnan, Iran

ARTICLE INFO

Keywords:
Photonic crystal
Ge2Sb2Te5
Waveguide intersection
Phase change material
Optical neuromorphic
Synapse

ABSTRACT

In this study, we propose an all-optical neuromorphic photonic crystal synapse structure equipped with a $Ge_2Sb_2Te_5$ phase-change material (GST-PCM). By leveraging the unique properties of the GST-PCM material, this structure enables the control of the synaptic weight through targeted and focused laser irradiation. 3D simulations employing the finite-difference time-domain (FDTD) and finite element method (FEM) demonstrated optical transmission exceeding 99 % and reflection below -20 dB at a wavelength of 1504 nm within the proposed structure. These features, together with their compact dimensions and low power consumption, make our proposed structure an ideal candidate for optical processing applications and neuromorphic neural networks. Furthermore, we investigated the physical and thermal equations to determine the crystallization fraction of GST-PCM during the synapse weighting process. These equations showed excellent agreement with the simulation results and could accurately calculate the GST-PCM crystallization fraction as a function of time and laser power. Our proposed structure not only has the potential to be extended to neuromorphic systems and optical neural networks but also serves as an innovative platform for all-optical synapses because of its precise control of optical properties, high adaptability, and low power consumption.

1. Introduction

The demand for modern computing, characterized by massive datasets and complex algorithms, has necessitated innovative approaches to information processing (Jauro et al., 2020). Inspired by the human brain, neuromorphic computing engineering (Burr et al., 2017) offers a promising solution by leveraging parallel processing, energy efficiency, and adaptive learning capabilities (Schuman et al., 2022). However, implementing these architectures using current electronic technologies faces challenges, such as limited bandwidth, high power consumption, and excessive heat generation (Tang et al., 2019; Huynh et al., 2022).

All-optical technologies, particularly those employing photonic crystal structures and phase-change materials, offer innovative solutions to these limitations (Nohoji et al., 2024; Laporte et al., 2018).

Due to their ability to provide ultrafast transmission and larger bandwidth compared to conventional electronic platforms, photonic technologies have gained significant attention in diverse domains such as high-speed data processing (Bednarkiewicz et al., 2023; Wang et al., 2022), optical neural networks (ONNs) (Xu et al., 2021), and optical

data storage (Hong et al., 2024). ONNs, inspired by the architecture of biological neural systems, leverage the advantages of optical signal manipulation and the intrinsic properties of photonic materials to boost computational efficiency (Hurtado et al., 2022; Xiang et al., 2021). Recently, these networks have emerged as powerful candidates for implementing advanced tasks such as adaptive learning, large-scale data handling, and memory functionalities within optoelectronic environments (Zhang and Tan, 2022). At the core of such systems lie optical synapses (Mahata et al., 2023; Lu et al., 2023; Yang et al., 2024; Zhou et al., 2024), which act as the fundamental building blocks for emulating brain-inspired learning and memory. These nanoscale photonic units process optical signals analogously to biological synapses and enable effective communication between artificial neurons, thereby ensuring efficient information transfer and interaction in optical neural architectures (Guo et al., 2021).

Photonic crystal structures are powerful tools for designing highperformance and compact optical systems owing to their unique ability to control light at the nanoscale. These structures enable precise guidance of light waves by creating photonic gaps and provide a suitable platform for designing optical synaptic architectures (Yadav et al.,

E-mail address: danaie@semnan.ac.ir (M. Danaie).

^{*} Corresponding author.

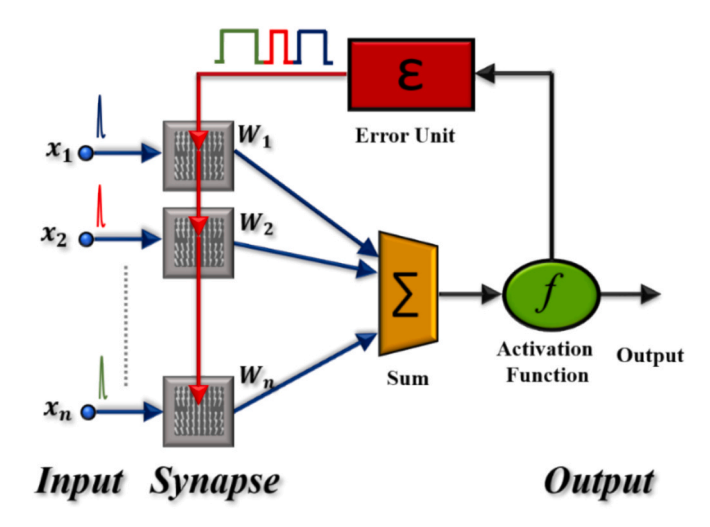


Fig. 1. Schematic of an artificial neuron with all-optical, tunable synapses. The neuron collects weighted input signals and processes them through an activation function to produce an output. The error block computes weight update signals to adjust the synaptic weights dynamically.

2021).

The realization of efficient optical synapses critically depends on the choice of materials whose optical parameters can be accurately manipulated (Fu et al., 2024). Among the various candidates, phase-change materials (PCMs) (Wang et al., 2023) have attracted significant attention, with Germanium-Antimony-Telluride (GST) (Wang et al., 2024) being one of the most widely investigated options. GST-based PCMs exhibit remarkable features such as rapid and reversible phase transitions, excellent thermal stability, and the capacity to encode multiple states, which makes them highly suitable for applications in optical memories (Lu and Yan, 2024), integrated photonic circuits, and, most importantly, optical synapses (Li et al., 2024; Zhang et al., 2024).

Using phase-change materials, such as $Ge_2Sb_2Te_5$ (Gerislioglu et al., 2020), in the architecture of all-optical structures is considered an essential step towards realizing flexible information processing and storage (Tao et al., 2024; Alkhamisi et al., 2022). These materials can undergo reversible phase transitions between amorphous and crystalline states with distinct optical properties that enable precise control of

synaptic weights (Guo et al., 2019; Wu et al., 2022; Qu et al., 2018).

Leveraging its non-volatile nature, GST has recently enabled the implementation of multiple photonic structures, including neuromorphic synapses (Zhuge et al., 2019; Xu et al., 2020), memory elements (Pernice and Bhaskaran, 2012) (Ríos et al., 2015), and optical switches (Rodriguez-Hernandez et al., 2017) (Stegmaier et al., 2017). These functionalities have been successfully integrated into devices such as Mach-Zehnder interferometers (Dhingra et al., 2019), ring resonators (Zheng et al., 2018), and photonic crystal (PhC) cavities (Ma et al., 2016).

Using laser radiation, it is possible to create stable changes in synaptic weights, which are the basis of the learning and memory processes in optical neural networks.

An important factor governing the performance of GST-based synapses in optical neural networks is the speed of this amorphous-to-crystalline switching. The dynamics of the transition have been widely reported: for instance, a switching time of $\sim\!32$ ns is demonstrated in (Kiselev et al., 2022), whereas a much faster transition of $\sim\!10$ ns is achieved in (Kunkel et al., 2022). These results confirm that GST possesses sufficient speed to be employed in ultrafast photonic devices. Nonetheless, despite these advantages, challenges remain regarding device longevity, as repeated cycling between the two phases can lead to gradual degradation, raising concerns about long-term reliability of GST in optical synaptic platforms.

All-optical neuromorphic synapses (Zhang et al., 2024; Prakash et al., 2022) offer an efficient solution for parallel and scalable processing in optical neural networks (Song et al., 2021; Feldmann et al., 2019). In these systems, light not only acts as an information-carrying signal but also as the main factor for adjusting synaptic weights, allowing for the design of more compact, faster, and more efficient circuits (Zhang et al., 2020; Tan et al., 2018). By mimicking biological synapses, these photonic counterparts are capable of performing complex computations with remarkable speed and precision, thereby significantly improving the performance of artificial intelligence systems and deep learning models (Huo et al., 2025; Luo et al., 2023).

Recently, several photonic synapse architectures based on phase-change materials have been proposed and actively investigated. For example, in (Nohoji et al., 2025), a photonic crystal waveguide intersection employing GST has been demonstrated as a neuromorphic synapse with a compact footprint of 29.16 μ m²; however, this design requires identical input wavelengths and weighting procedures across

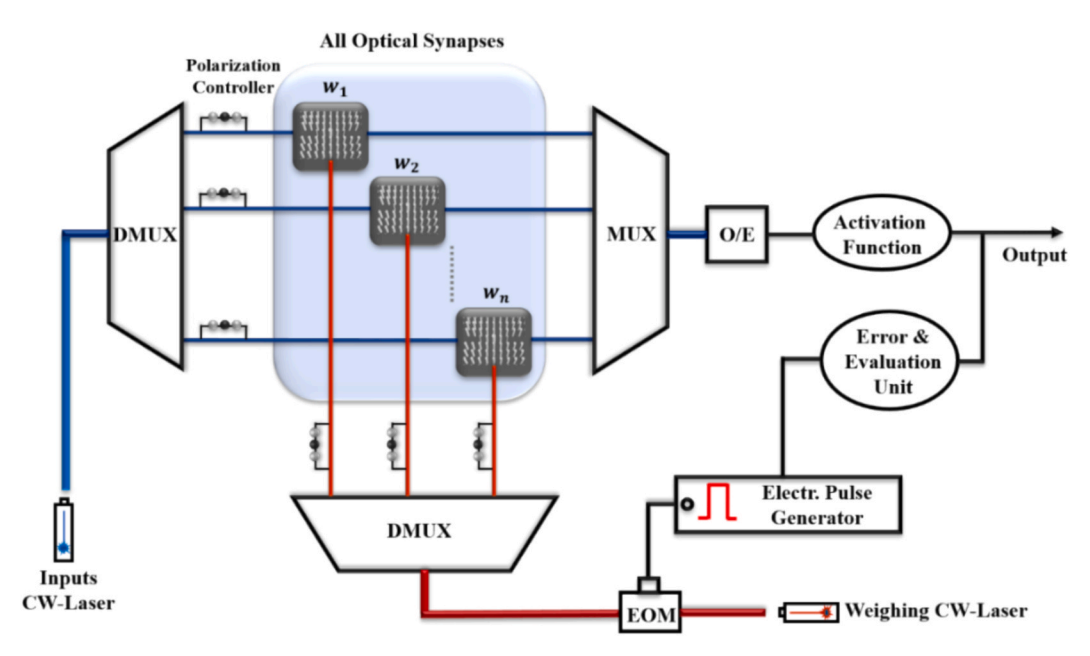


Fig. 2. The architecture of an artificial neuron using all-optical synapses.

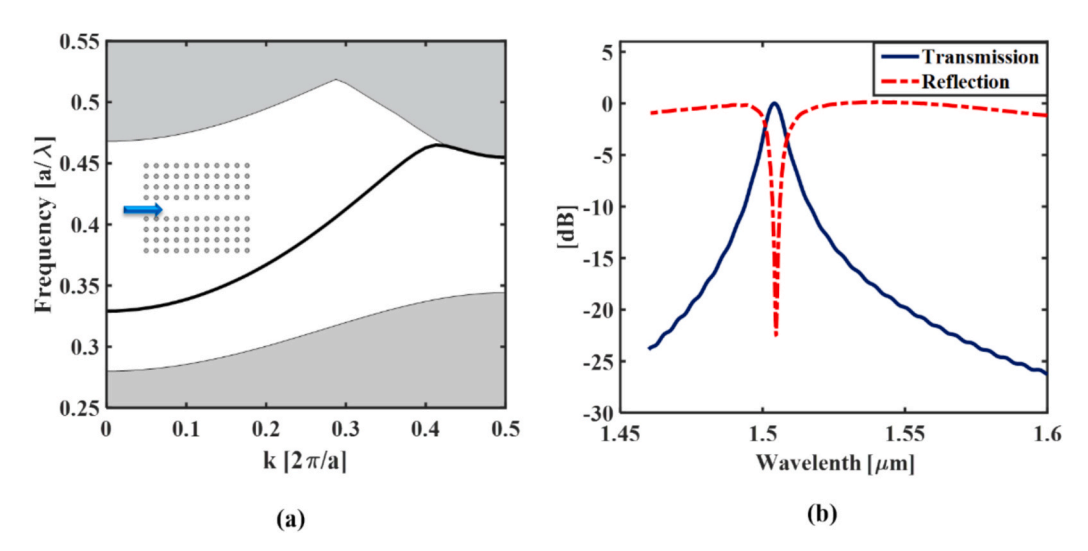


Fig. 3. (a) Band structure of the proposed photonic crystal waveguide in normalized frequency. (b) Transmission and reflection in dB.

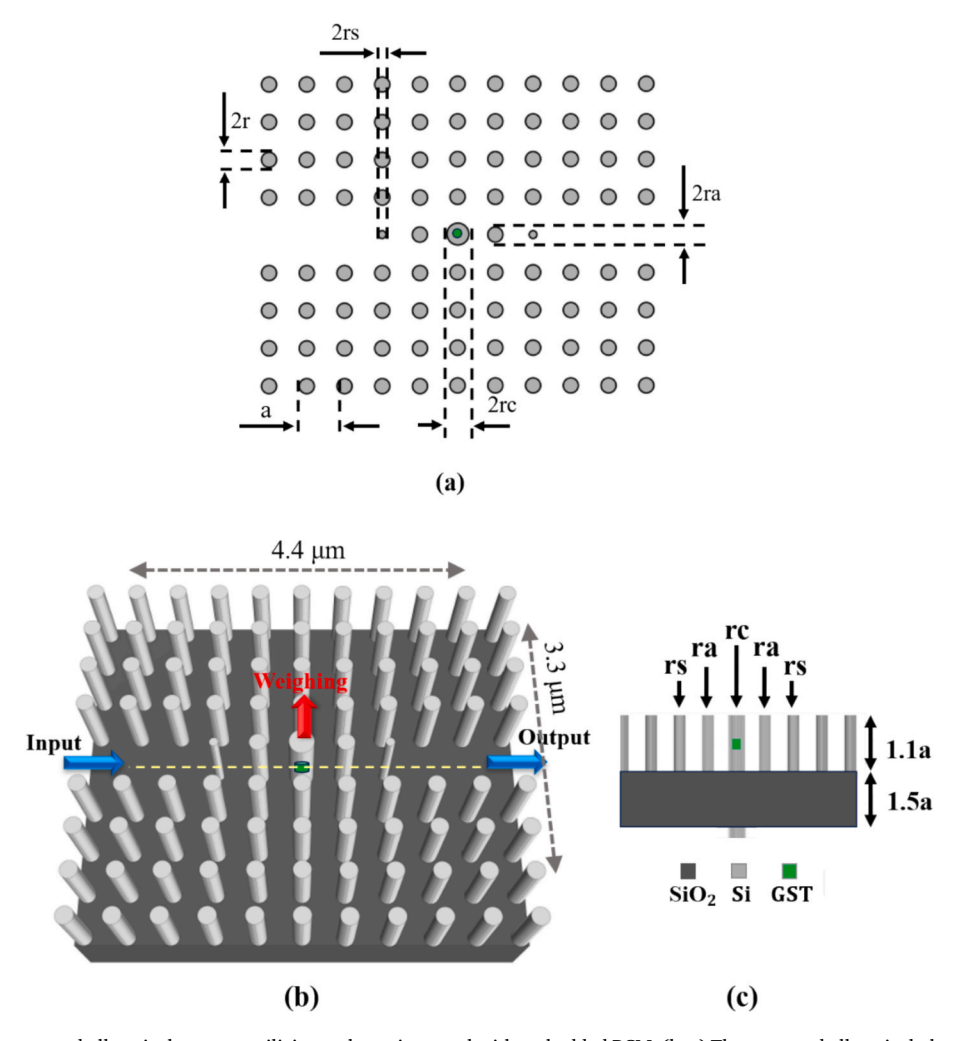
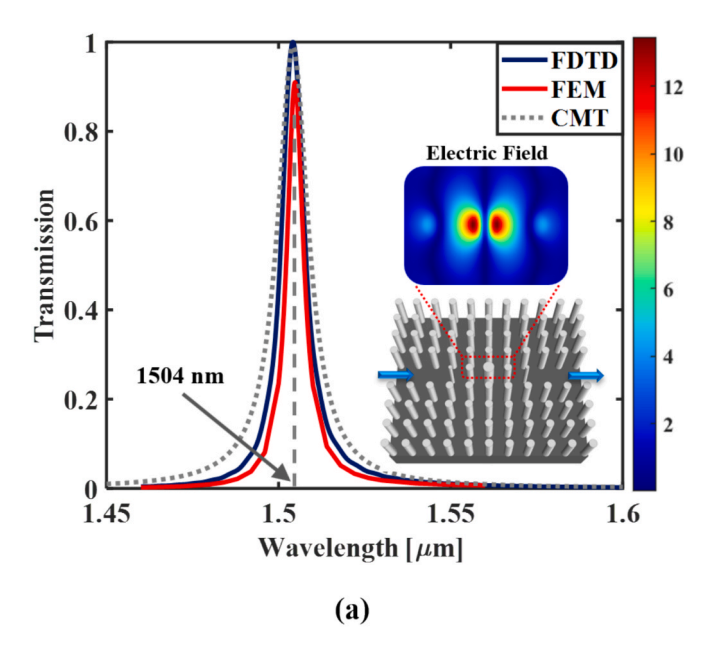


Fig. 4. (a) 2D view of the proposed all-optical synapse utilizing a photonic crystal with embedded PCM. (b, c) The proposed all-optical photonic crystal synapse. Blue arrows represent the input and output optical paths, and red arrows depict the weighting signal path used to adjust synaptic weights. (For interpretation of the references to colour in this figure legend, the reader is referred to the web version of this article.)

all synapses. In (Nohoji et al., 2025), a Mach-Zehnder interferometer integrating directional couplers with GSST has been reported, occupying an area of $195~\mu\mathrm{m}^2$, where the weighting operation relies on injecting inphase and equal-amplitude signals into both couplers. Moreover, in

(Nohoji et al., 2025), a slab-type photonic crystal with a triangular lattice of air holes has been investigated, exhibiting an energy consumption of 267 pJ per synaptic weighting operation.

In this study, we propose an all-optical photonic crystal synaptic



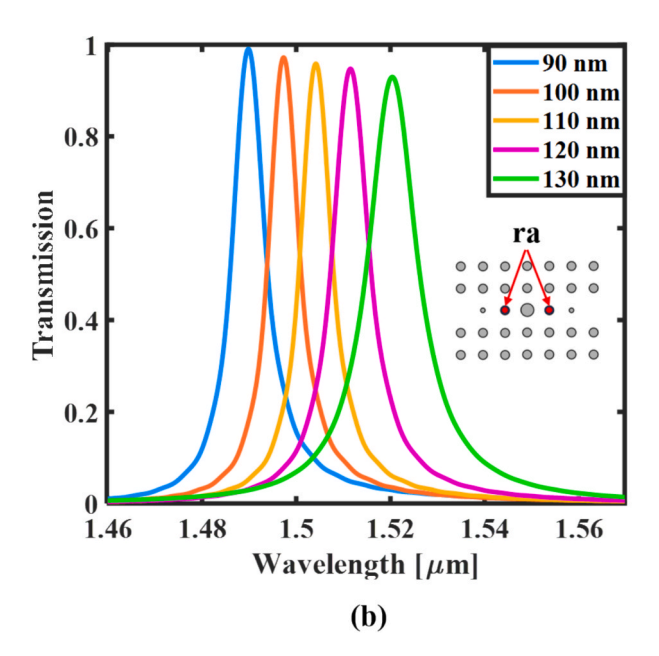


Fig. 5. (a) Comparison of transmission using FDTD, FEM simulations, and CMT. All three methods show good agreement. (b) Comparison of transmission for rod radius rs in the range of 90 and 130 nm.

structure based on GST-PCM for implementation in optical processing systems and neural networks. By exploiting the photonic band gaps in photonic crystals and integrating them with GST materials, our proposed structure enables the precise control of light emission and dynamic tuning of synaptic weights. In this structure, the synaptic weight is controlled only by precisely engineered laser radiation, which facilitates learning and memory processes.

Comprehensive 3D simulations show that the proposed structure is highly accurate and fully respects basic physical principles. In addition, the use of photonic crystal structures allows the design to be optimized with a significant reduction in size and power consumption compared to conventional models.

Our findings demonstrate that the proposed all-optical neuromorphic synapse design offers substantial reductions in power consumption, enabling more compact system footprints, and enhancing the scalability of neuromorphic neural network architectures. This development represents a significant milestone in the advancement of information processing systems, paving the way for the realization of efficient small-scale implementations of all-optical neuromorphic systems.

2. An artificial neuron structure

Fig. 1 shows the block diagram structure of an artificial neuron. In this structure, input signals pass through channels x_1 to x_n , and the corresponding synapses adjust the weight of the input signal. The sum block then aggregates the weighted inputs and applies the resulting output to an activation function (Karlik and Olgac, 2011). This nonlinear mathematical function that plays a vital role in enabling the complex and nonlinear behaviors of neural networks (Ramchoun et al., 2016; Du et al., 2022). This function is usually defined as a sigmoid or ReLU function (Waoo and Soni, 2021; Dubey et al., 2022), so that if the sum of the weighted inputs exceeds a certain threshold, the neuron produces an output signal.

The neuron uses learning algorithms such as error backpropagation (Henseler, 2005) or delta law (Chakraverty et al., 2019; Auer et al., 2008) to optimize the network performance and minimize errors. These algorithms work on the principle of error reduction. In this process, the neuron compares the obtained output with a reference or target value in the error block and, based on the calculated error, sends corrective signals to the synapses to adjust the synaptic weights. This process gradually reduces the output error with each iteration, leading to training of the neural network. In this way, the network gradually learns and can generalize to new inputs.

The detailed steps this algorithm are formulated based on the neural network learning flow, which outlines the interconnections among system components and describes how the network gradually minimizes its error through iterative weight adaptation.

Neural network learning flow:

Input Initialization: The process begins by providing the neuron with an input vector $\{x_i\}$. Each element of the vector represents a synaptic input signal.

Weighted Summation: The input signals are multiplied by their corresponding synaptic weights $\boldsymbol{w}_i^{(k)}$, where k denotes the current training epoch. The neuron's internal potential is obtained as:

$$S = \sum_{i=1}^{n} x_i w_i^{(k)} \tag{1}$$

Activation: The summation result is processed through a nonlinear activation function $f(\cdot)$, yielding the neuron output at epoch k:

$$O^{(k)} = f(S) \tag{2}$$

Error Computation: The deviation between the actual neuron output and the desired (target) output P is quantified using the mean-squared error criterion:

$$E_r = \frac{1}{2}(O^{(k)} - P)^2 \tag{3}$$

Convergence Check: If the error E_r falls below a predefined tolerance, the training process is terminated. Otherwise, weight adaptation is performed.

Gradient Evaluation: The gradient of the error function with respect to each synaptic weight is computed according to the delta rule:

$$\Delta w_i^{(k)} = \frac{\partial E}{\partial w_i^{(k)}} \tag{4}$$

Weight Update: Synaptic weights are updated via the gradient-descent learning rule, incorporating the learning rate α :

$$\mathbf{w}_i^{(k+1)} = \mathbf{w}_i^{(k)} - \alpha \Delta \mathbf{w}_i^{(k)} \tag{5}$$

Iteration: The epoch index is incremented $(k \rightarrow k + 1)$, and the

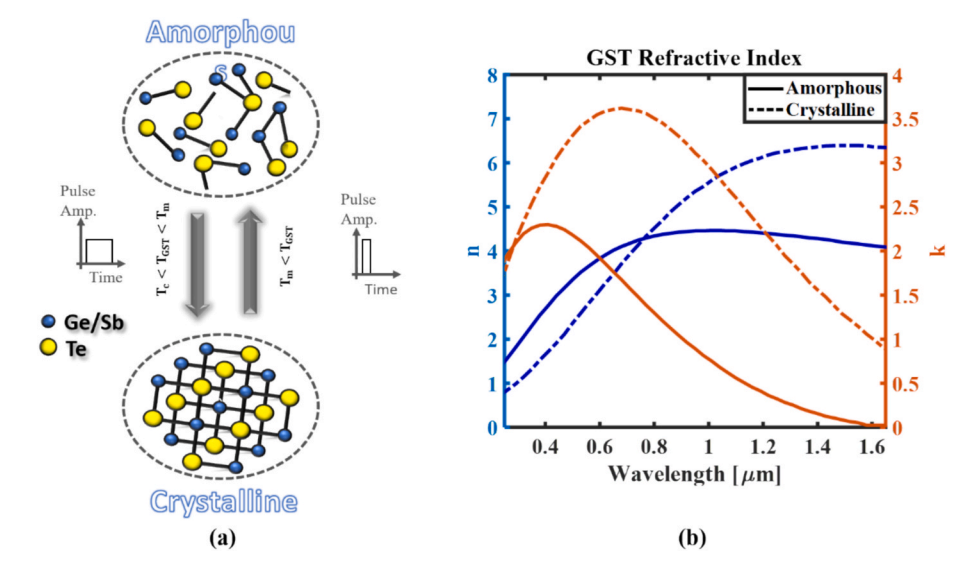


Fig. 6. (a) Crystalline-Amorphous Phase Transition in GST-PCM. By applying long-duration, low-amplitude laser pulses, the temperature of GST-PCM can be controlled in a range between the crystallization temperature (T_c) and the melting point (T_m). (b) The real and imaginary parts of the refractive index of GST-PCM in fully amorphous and crystalline states at different wavelengths.

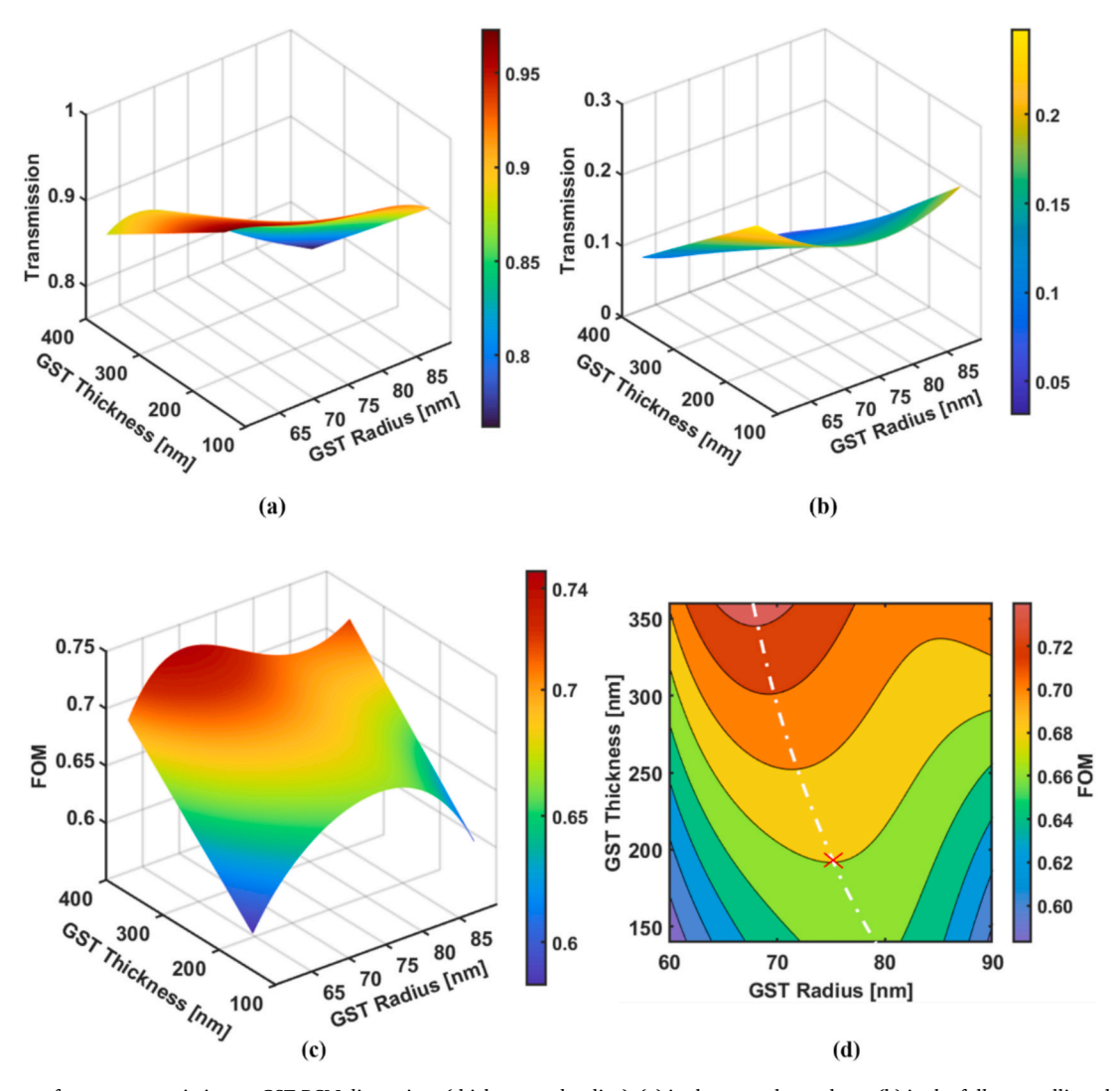
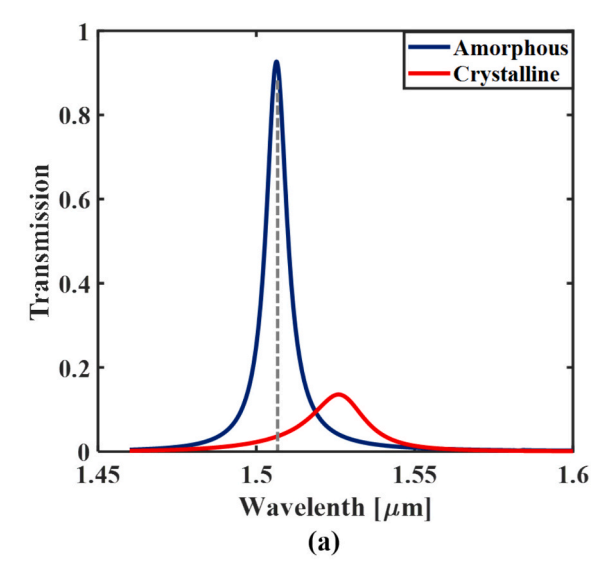


Fig. 7. Dependence of output transmission on GST-PCM dimensions (thickness and radius), (a) in the amorphous phase, (b) in the fully crystalline phase, (c) in terms of the figure of merit, (d) Contour plot of FOM. The thickness and radius of GST-PCM are chosen to be 200 nm and 75 nm, respectively.



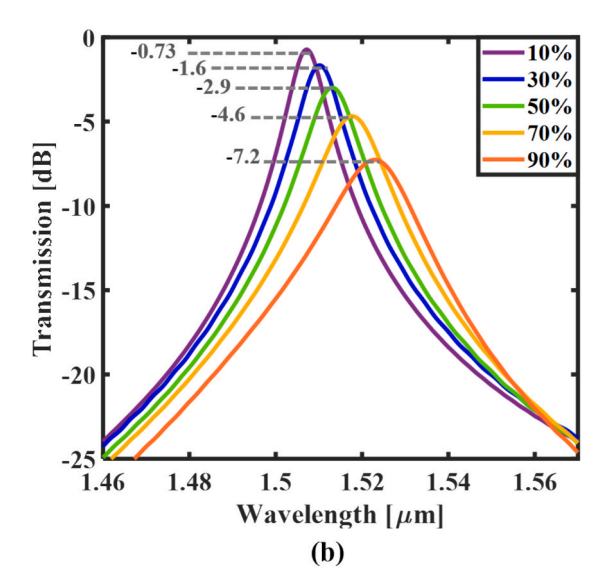


Fig. 8. (a) Transmission comparison between amorphous and fully crystalline GST-PCM states, (b) transmission variation for crystallization fractions ranging from 10~% to 90~%.

procedure is repeated until the convergence criterion is satisfied.

Fig. 2 shows the structure of a neuron with all-optical synapses designed to implement neuromorphic neural network processing. In this structure, a continuous wave (CW-laser) laser generates inputs at different wavelengths and transmits them (via the blue path) to the multiplexer block (DMUX). The DMUX block is responsible for separating and adjusting the polarization, and sending each incoming wavelength to the all-optical synapse. Synapses give weight to the incoming wavelengths.

After the weighting process, a multiplexer (MUX) block combines the weighted input wavelengths. It feeds them an optical-to-electrical (O/E) module to convert them into electrical signals (via the black path). The (O/E) module feeds the resulting electrical signals into a nonlinear activation function block. This block analyzes signals and determines the final output of the neuron.

Subsequently, an error evaluation block compares the obtained output with the target value and calculates the synaptic correction coefficients. Subsequently, an electro-pulse generator generates synapse weight correction pulses. An electro-optic modulator (EOM) converts these pulses into optical signals and sends them through red paths to the

DMUX block to be applied to the corresponding optical synapses after polarization adjustment.

3. All-optical proposed synapse structure

The proposed synaptic structure utilizes silicon rods embedded in a square photonic crystal lattice on a SiO_2 substrate. The lattice constant of this structure was set to a $=0.55~\mu m$. The rods were designed with a height of 1.1a, and the SiO_2 thickness was set at 1.5a, carefully selected to optimize light confinement and minimize optical losses.

Fig. 3(a) shows the band structure of the proposed photonic crystal waveguide. The band gap of this waveguide lies within the normalized frequency range of 0.33 to 0.46. This transmission range validates the suitability of the structure for various photonic applications.

To create a high-transmission waveguide, one row of rods was removed from the structure, and the radii of the five central rods were precisely adjusted and optimized. The central cavity rod is set to $r_{\rm c}=0.29a$, while the radius of the surrounding rods was adjusted between 90 and 130 nm. This precise adjustment allows for accurate control of the transmitted wavelength and optimizes the overall optical performance of the structure.

Two scattering rods (r_s) were placed at the waveguide path to enhance the quality factor (Q-factor) (Nohoji and Danaie, 2022). These rods improve the overall performance by minimizing reflection losses and maximizing light confinement.

Optical response of the proposed photonic crystal structure in terms of reflection and transmission spectra is presented in Fig. 3(b). The results, obtained under TM polarization, indicate a reflection level below –20 dB at the operational wavelength of 1504 nm, confirming the efficient light propagation through the structure.

One of the distinctive characteristics of the proposed structure is its capability to dynamically control the intensity of transmitted light by exploiting the thermo-optic properties of a PCM situated at the core of the central cavity rod. By applying a vertical laser to the central rod (r_c), the rod acted as an optical fiber, guiding light into the embedded PCM. The incident light increases the temperature of the PCM, resulting in a change in its refractive index. This refractive-index modulation enables precise control of the light transmission characteristics within the waveguide.

Fig. 4 shows the proposed structure, which is specifically designed to function as an all-optical synapse in neuromorphic neural networks. The ability to precisely adjust rod radii enables fast response times and seamless integration with other optical components, making it a promising candidate for advancing the fields of optical computing and neuromorphic artificial intelligence.

Fig. 5(a) shows the structure transition without a PCM. The results show that the structure has a transmission of 99 % at a wavelength of 1504 nm. This characteristic demonstrates the optimized performance of the structure at the designated wavelength and its effectiveness in mitigating reflection losses. Moreover, the cavity structure exhibits a narrow full width at half maximum (FWHM) of 7.7 nm and a Q-factor of 195 at the transmission wavelength. To validate the simulation results, the proposed structure we investigated using three methods: FDTD, FEM, and coupled-mode theory (CEM).

The cavity resonances can be effectively modeled using coupled mode theory by analyzing the interaction between the waveguides and the cavity. The transfer function associated with the input and output of waveguides connected to the cavity is expressed as a function of the cavity Q-factor, which is related to the intrinsic loss of the cavity and the coupling strength between the waveguide and cavity (Asgari and Fabritius, 2020). The transfer function is defined in Eq. (6) (Akahane et al., 2005; Li et al., 2010):

$$tf = \frac{\frac{1}{Q_w}}{\frac{1}{Q_l} + \frac{2j}{Q_w} + \frac{2j}{\lambda_n}} \tag{6}$$

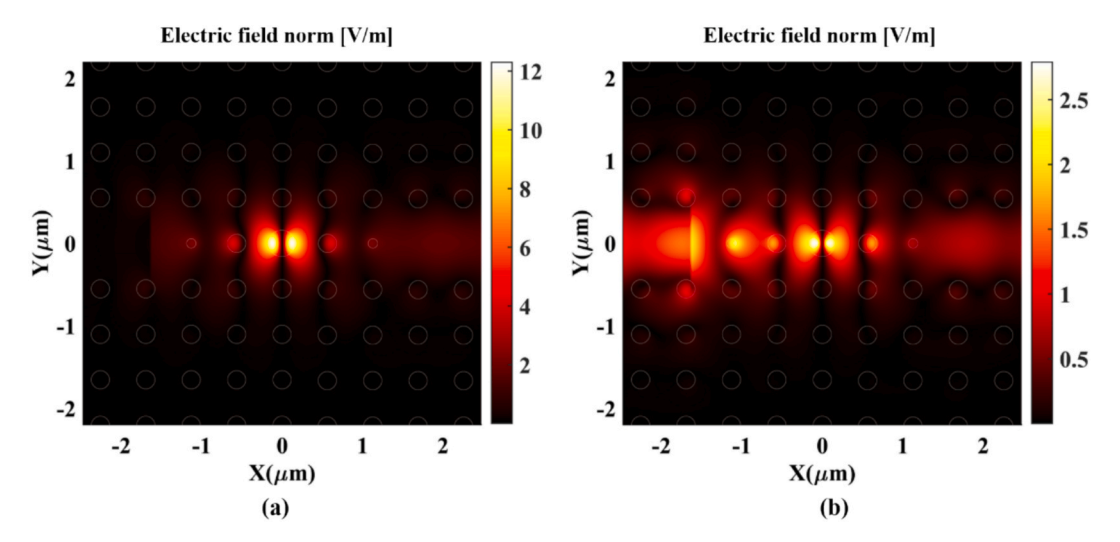


Fig. 9. Electric field profiles of the proposed structure using GST-PCM in (a) amorphous and (b) fully crystalline phases. The amorphous phase exhibits minimal optical absorption and maximum transmission, while the crystalline phase shows increased absorption and reduced transmission.

Amorphous

3

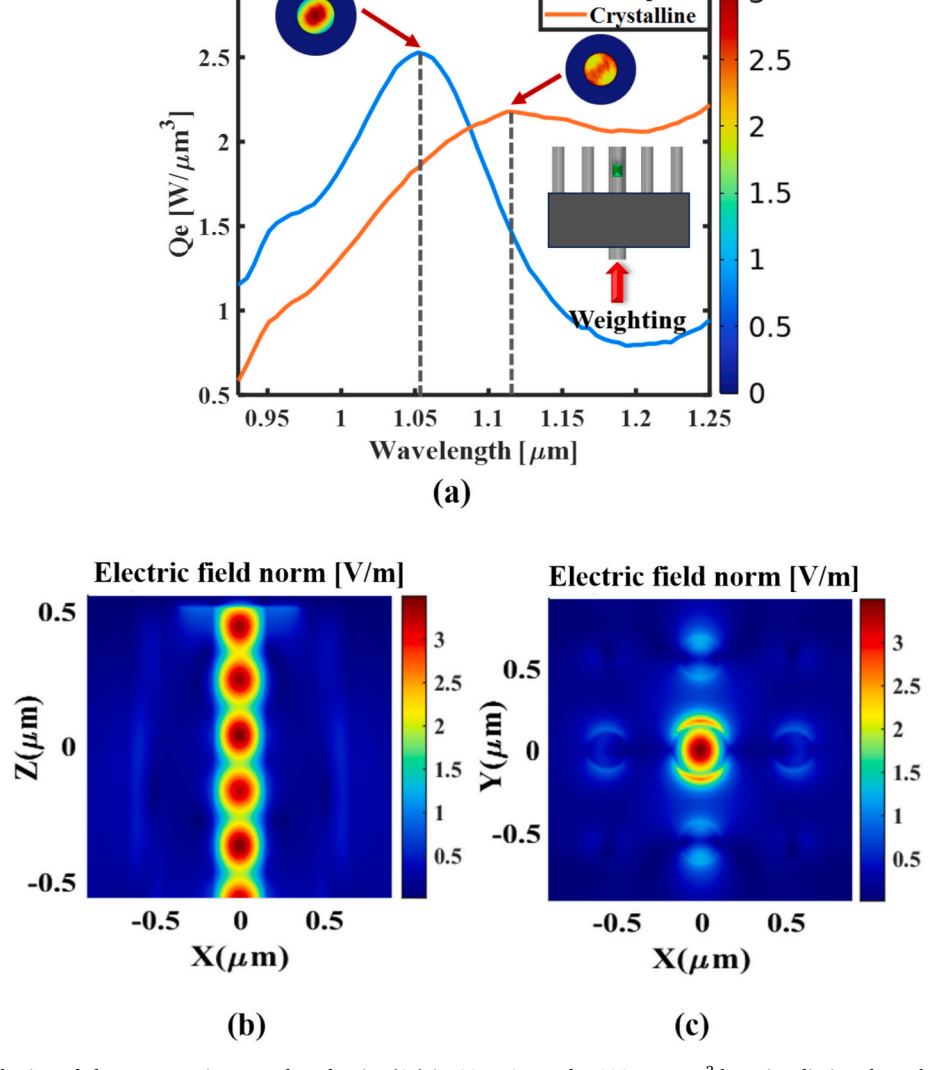
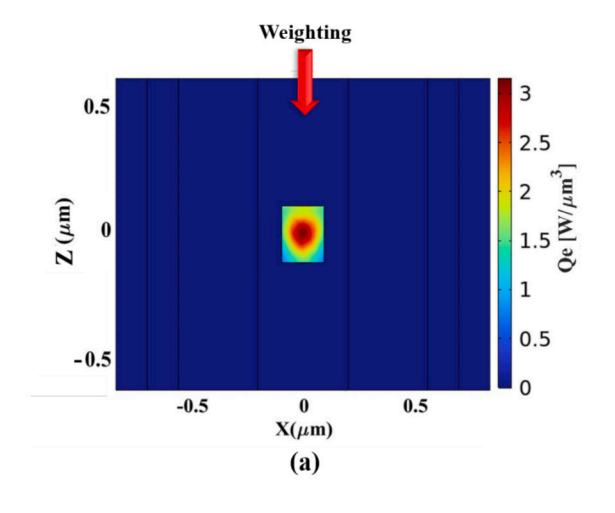


Fig. 10. (a) Spectral distribution of electromagnetic power loss density (Q_e) in GST-PCM under 100 mW/ μ m² laser irradiation through the central cavity rod (r_c) . Maximum Q_e occurs at 1.05 μ m for amorphous and 1.12 μ m for crystalline phases. (b, c) Electric field profile in the cavity structure without the GST-PCM under laser irradiation from the central rod.



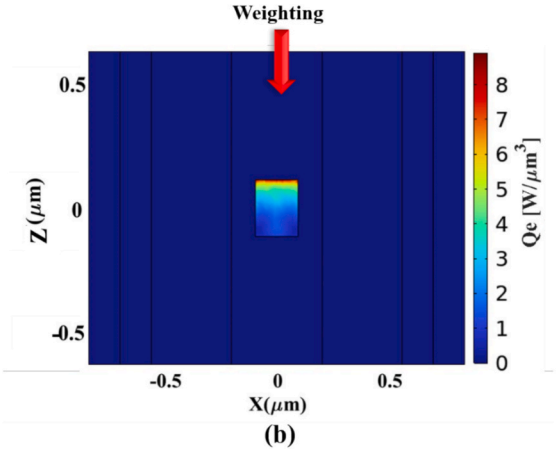


Fig. 11. Distribution of power loss density Q_e in GST-PCM under $100 mW/\mu m^2$ laser irradiation for (a) amorphous phase and (b) fully crystalline phase. In the crystalline phase, the Q_e is predominantly absorbed at the surface of the GST-PCM.

and λ_n is defined as Eq. (7).

$$\lambda_n = \frac{\lambda}{\lambda_0 - \lambda} \tag{7}$$

where λ_0 is the cavity resonance wavelength.

The quality factors associated with the cavity and coupling are related to the intrinsic cavity loss (τ_i) and coupling loss to the waveguide (τ_w) , respectively, and are detailed in Eq. (8) and Eq. (9).

$$Q_i = \frac{\pi C \tau_i}{\lambda_0} \tag{8}$$

$$Q_{w} = \frac{\pi C \tau_{w}}{\lambda_{0}} \tag{9}$$

Where *C* is the speed of light.

Furthermore, Eq. (10) determines the transmission (Tr) through the cavity waveguide structure (Li et al., 2010).

$$Tr = |tf|^2 \tag{10}$$

For the proposed structure, we obtained the values of Q_i and Q_w values of 27,382 and 138, respectively.

Fig. 5(a) presents a comparative analysis of the results obtained from the three simulation methods, revealing a high degree of consistency. The observed 8 % deviation in the transfer parameter was due to the difference in the distinct meshing strategies employed in the two

simulation methods. This discrepancy is mainly due to changes in the geometric precision and discretization of the computational domain. The strong correlation between the results of the three methods (FEM, FDTD, and CMT) proves the accuracy of the simulations. It emphasizes the robustness of the proposed structure for practical applications.

For the FDTD simulations, perfectly matched layer (PML) boundary conditions were applied to all boundaries to minimize reflections. A grid resolution of 10 nm was used to accurately capture variations in the electromagnetic field. Convergence was ensured using the Auto Shutoff feature, such that the total field energy decayed to less than 10^{-5} of its initial value.

As shown in Fig. 5(b), a tunable transmission spectrum can be realized by systematically varying the radius of the scattering rods (r_s) in the range 90–130 nm. This capability enables precise tuning of the transmission wavelength for each synapse, thereby providing a mechanism to optimize the neuromorphic synaptic performance tailored to specific optical system requirements.

3.1. Ge₂Sb₂Te₅ phase-change material

Phase-change materials have gained attention in recent years as applied elements in optical and optoelectronic technologies. These materials possess unique properties that make them ideal for applications in phase-change memory and programmable optical systems. Germanium-antimony-telluride (GST), one of the best-known PCMs, exhibits remarkable optical and electromagnetic properties owing to its ability to reversibly switch between amorphous and crystalline phases. This material has numerous applications, including optical data processing, data storage, and all-optical neuromorphic systems.

All-optical neuromorphic systems use GST-PCM as the basic material to simulate biological synaptic functions (Pernice and Bhaskaran, 2012; Chakraborty et al., 2019; Chakraborty et al., 2018; Brückerhoff-Plückelmann et al., 2021). By leveraging the unique properties of GST-PCM, synaptic attributes such as weight modifications can be precisely and rapidly controlled through optical means. This capability promises significant advances in optical data processing for neuromorphic neural networks.

The phase transitions in GST-PCM, commonly instigated by thermal or optical stimuli (Bakan et al., 2016), can modulate the optical properties of the material, thereby affording precise control over the light transmission characteristics, including the refractive index, absorption, and reflection in different phases. This capability enables complex optical processing at the micro-scale and high speeds. As a result, GST-PCM is extensively employed to design optical synapses and neuromorphic systems, especially in applications demanding optical data processing and storage. Furthermore, the exploitation of GST-PCM in optical systems, including tunable filters (Julian et al., 2020; Gnawali et al., 2024), sensors (Zou et al., 2019; Mondal, 2008), switches (Elliott, 2015; Cao et al., 2020), and optical processors (Kumar and Sharma, 2020; Du, 2022), has facilitated significant advances in various optical technologies.

The crystallization fraction of GST-PCM (η) was modulated by increasing the temperature through a thermal or optical source, as shown in Eq. (11) (Nohoji et al., 2024; Rashidi et al., 2021; Rashidi et al., 2023). These temperature fluctuations induce substantial alterations in the optical properties of GST-PCM, notably its refractive index (Feldmann et al., 2019). The refractive-index changes caused by the GST-PCM phase transition have significant advantages for applications in optical neuromorphic systems, including learning processes and synaptic weight tuning. According to the Lorentz-Lorenz equation (Rashidi et al., 2021; Pourmand and Choudhury, 2022) (Eq. (12)), the refractive index of the PCM exhibits a nonlinear dependence on the variation in the crystal fraction. This nonlinear behavior has a significant impact on the light transmission in PCM-based systems and plays an important role in controlling and optimizing the performance of these systems.

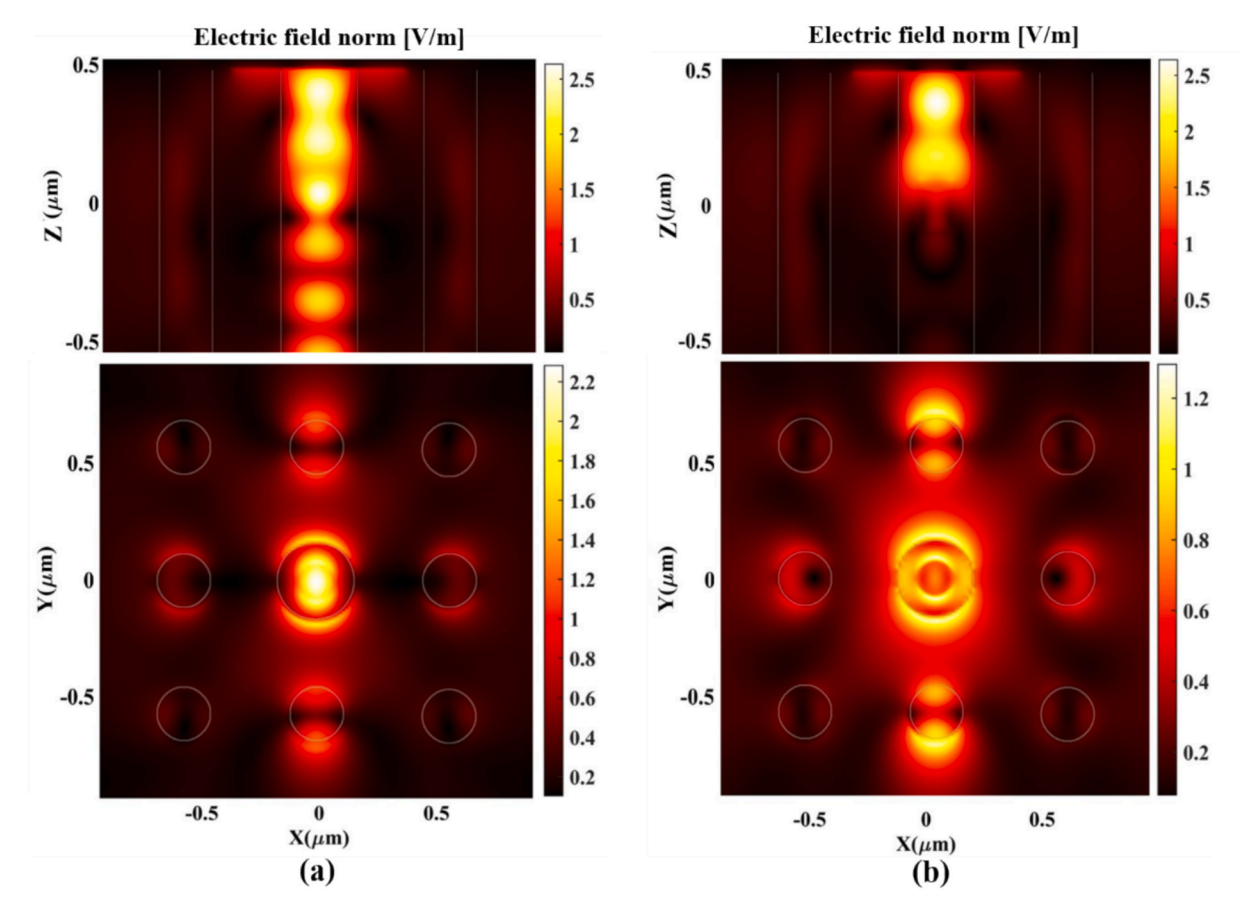


Fig. 12. Electric field profiles in the GST-PCM for (a,) the amorphous phase and (b) the fully crystalline phase.

$$\eta(T) = \frac{e^{(\frac{T_{0}_{kelvin} - 615}{30})}}{1 + e^{(\frac{T_{0}_{kelvin} - 615}{30})}}$$
(11)

$$\varepsilon_{\it eff-GST}(\eta) = \frac{\varepsilon_{\it am} \big(\varepsilon_{\it cry} + 2\big) + 2\eta(\varepsilon_{\it cry} - \varepsilon_{\it am})}{\varepsilon_{\it cry} + 2 - \eta(\varepsilon_{\it cry} - \varepsilon_{\it am})} \tag{12}$$

where ε_{cry} and ε_{am} are crystallization and amorphous permittivity of GST-PCM, respectively.

Using a light pulse of appropriate power and duration allowed modulation of the GST-PCM crystallization fraction in the range of 0 to 1. This facilitates the gradual transition of the material between the amorphous and crystalline phases. This capability is important for programmable optical systems and optical neuromorphic synapses.

Furthermore, applying high-power, short-duration light pulses enabled the rapid quenching of GST-PCM from the crystalline to the amorphous state. These features, along with their high compatibility, make GST-PCM an exceptional choice for use in optical memory systems and dynamic synaptic weight tuning. These capabilities are essential for the learning and adaptation of optical neural networks (Fig. 6(a)).

Fig. 6(b) shows the dependence of the changes in the real and imaginary components of the refractive index of GST-PCM (Feldmann et al., 2019). These changes are not only critical for optical systems and switches, but also serve as a key tool in the design of neuromorphic synapses at the micro- and nanoscale. These features allow for more precise engineering of the optical and dynamic properties of these structures, helping to facilitate advanced applications in new optical technologies.

3.2. Synapse structure utilize GST-PCM

As shown in Fig. 4, the GST-PCM element was strategically

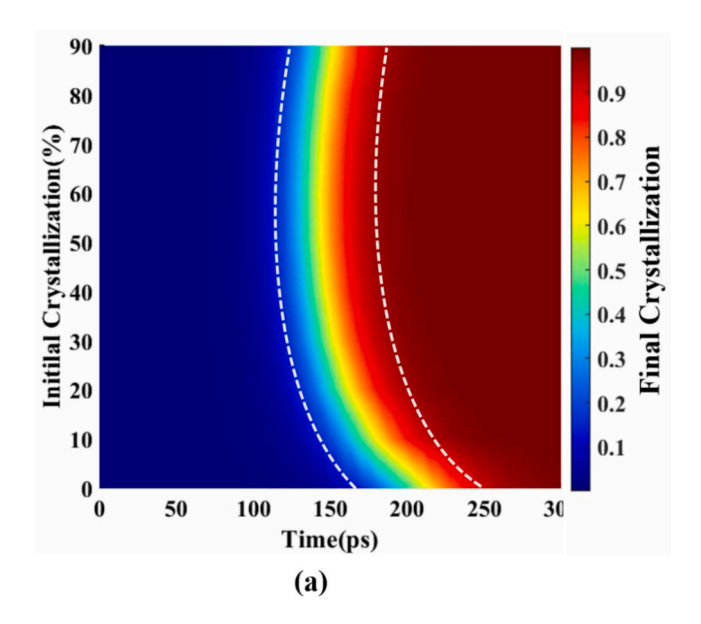
incorporated into the central cavity rod. To systematically assess the influence of rod dimensions on structural performance, the radius and height of the GST-PCM element were parametrically varied. Fig. 7(a, b) show that the amorphous phase provides maximum transmission and the crystalline phase provides minimum transmission through the structure. To quantitatively assess the influence of the central rod geometry, we defined the figure of merit (FOM) according to Eq. (13). The calculated FOM values for the different radius and thickness combinations are shown in Fig. 7(c). As shown in Fig. 7(d), the FOM exhibited a positive correlation with the rod thickness. However, this increase is accompanied by a concomitant increase in the input power required to facilitate the phase transition from the amorphous to crystalline state, which is undesirable because of practical limitations and energy efficiency considerations. Therefore, an FOM of 66 % was selected, corresponding to a GST-PCM rod radius of 75 nm and thickness of 200 nm, to optimize device performance while balancing power efficiency and optical performance.

$$FOM = \frac{T_{ram} - T_{rcry}}{T_{ram} + T_{rcry}} \tag{13}$$

 T_{rcry} and T_{ram} represent the crystalline and amorphous state transitions of the GST-PCM, respectively.

Fig. 8(a) shows the contrasting transmission characteristics of the structure in the amorphous and crystalline phase states of the GST-PCM. The amorphous phase exhibited a significantly higher transmission than the crystalline phase. Fig. 8(b) depicts the output transmission as a function of the crystallization ratio (in dB). The plot clearly illustrates the gradual modulation of the transmission characteristics in response to incremental changes in the crystallization ratio, thus confirming the tunability and precise control of the optical properties of the system.

In addition to the changes in the imaginary part of the refractive



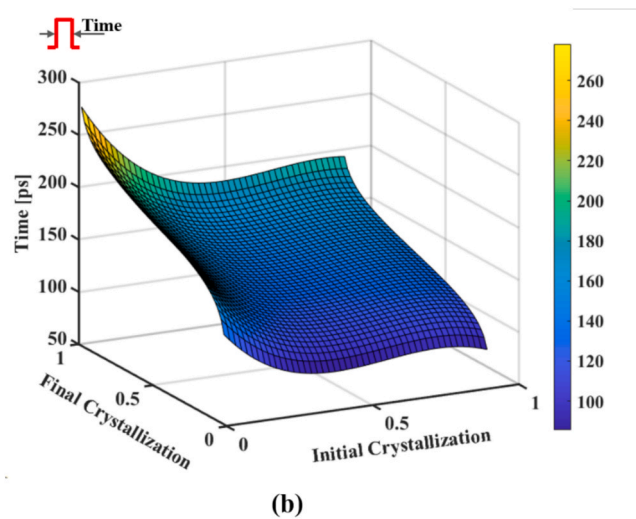


Fig. 13. (a) Effect of 100 mW/μm² laser pulse duration on the crystallization fraction of the GST-PCM. The graph shows the variation in the crystallization fraction of the GST-PCM as a function of laser pulse duration and the initial crystallization fraction. The region between the two white dashed lines represents the range of crystallization fraction changes from 0 % (amorphous phase) to 100 % (fully crystalline phase). (b) Required 100 mW/μm² laser pulse duration for complete GST-PCM crystallization as a function of the initial crystallization fraction.

index (related to signal absorption), the phase transition of GST-PCM from the amorphous to crystalline state also leads to an increase in the real part of the refractive index. As the real part of the refractive index of GST-PCM increases, the transmission peak shifts to longer wavelengths. Consequently, considering a fixed incident laser wavelength at the amorphous state peak of GST, the transmission can be tuned over a wide range from 93 % to 5 %. This high degree of tunability makes the proposed GST-based structure ideal for implementation as a fully optical synapse with precise controllability in neuromorphic circuits.

Fig. 9 shows the electric field profiles within the structure of the amorphous and crystalline phase states of GST. These profiles demonstrate significant differences in how light interacts with GST material in each phase state.

4. Weighting mechanism

In this study, we used an innovative fiber-optic-inspired technique to precisely tune the crystalline fraction of GST-PCM embedded in the central rod (rc). A vertical pulse was launched into the structure and was guided along the central rod. By adjusting the power and duration of the pulse applied to GST-PCM, the crystallization fraction could be precisely adjusted.

To determine the optimal wavelength for adjusting the crystallization fraction, we evaluated the Q_e parameter of the GST. Fig. 10(a) illustrates the variation in Q_e for both the crystalline and amorphous phases of the GST-PCM. The results revealed that the optimal wavelength for effectively modulating the crystallization ratio in the amorphous phase is 1.05 μm , where Q_e reaches its maximum value.

Fig. 10(b) and (c) show the electric field distribution profiles of the proposed structure without GST-PCM under excitation with a 1.05 μm wavelength laser emitted from the central rod (r_c). These profiles accurately demonstrate the impact of an external laser wave on the optical fields and the structural and transmission properties of the system.

Fig. 11 shows the distribution of the electromagnetic power loss density at a wavelength of 1.05 μm in the amorphous and crystalline phases of the GST-PCM. Furthermore, the electric field profiles within the structure for both the amorphous and fully crystalline phases under the excitation of the weighting wavelength (1.05 μm) are illustrated in Fig. 12.

Fig. 13(a) illustrates the time-dependent evolution of the GST-PCM crystallization fraction under different initial crystallization conditions when exposed to an irradiation intensity of 100 mW/ μ m² from the central rod. The results demonstrate that the time required for the complete crystallization of GST-PCM remains nearly constant, irrespective of the initial crystallization state (the distance between the two white dashed lines). These results indicate that the duration of the input laser irradiation for the complete crystallization of GST-PCM is mainly independent of the initial conditions of the GST-PCM crystallization fraction, which facilitates the calculation of pulse duration settings and the optimization of learning processes in optical neuromorphic systems. However, the time required to apply a laser pulse to GST-PCM to reach the critical temperature and initiate crystallization varies with the initial crystallization fraction, and these changes must be carefully considered in the design and precise control of neuromorphic synapse processes.

Fig. 13(b) depicts the time required to determine the crystallization ratio of the GST material when irradiated with a 100 mW/ μ m² pulse through the central rod for weighting GST-PCM. The crystallization time was derived using an interpolation method based on Eqs. (14–16). This allowed for precise adjustment of the 100 mW/ μ m² laser irradiation time to achieve the desired crystallization ratio in the GST material. This approach offers a practical method for controlling the crystallization process and tailoring the optical properties of the device.

$$\mathit{Time}[ps] = \frac{0.1Y}{I_{in}\left[W/\mu m^2\right]} \tag{14}$$

and

$$Y = A + B\eta_0 + CT + D\eta_0^2 + ET\eta_0 + F\eta_0^3 + GT\eta_0^2$$
(15)

and

$$T = 30\ln\left(\frac{\eta}{1-\eta}\right) + 615\tag{16}$$

where η_0 is the initial crystallization fraction, and the coefficients *A*, *B*, *C*, *D*, *E*, *F* and *G* are -167.7, -16.5, 0.6094, 394.1, -0.6131, -389.6 and 0.5066, respectively.

As a result, the processing unit responsible for setting the weight in each neuron can calculate the laser pulse length using Eq. (14), and subsequently send a laser pulse of a specified duration to the GST-PCM



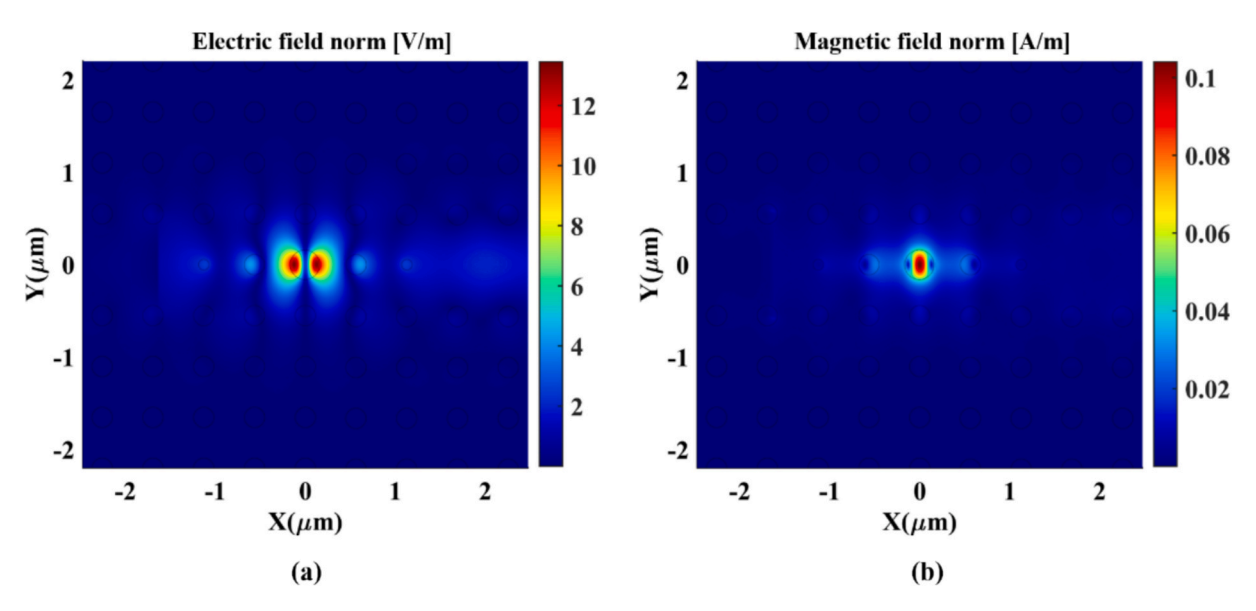


Fig. 14. (a) Electric field profile and, (b) magnetic field profile of all-optical proposed synapse structure at 1504 nm wavelength.

Table 1
Material parameters.

Material	n	k	ρ [kg/m ³]	k [w/m.k]	C_p [J/K. kg]	
Silicon (Yamasue et al., 2002; Aspnes and Studna, 1983; Laprais et al., 2024)	3.5	0	2330	148	711	
Air (Rodrigues et al., 2021)	1	0	350–1225	0.026-0.076	1100	
Silicon dioxide (Zhu et al., 2018; Laprais et al., 2024; Malitson, 1965)	1.47	0	2203	1.4	709	
GST-am (Feldmann et al., 2019; Chakraborty et al., 2018; Zhu et al., 2018)	(Feldmann et al., 2019)	(Feldmann et al., 2019)	5870	0.19	217	
GST-cry (Feldmann et al., 2019; Chakraborty et al., 2018; Zhu et al., 2018)	6.39	1.26	6270	0.59	217	

in the proposed synapse structure. This technique not only optimizes the performance of neuromorphic systems but also increases the accuracy and efficiency of adjusting the transmission speed and weight in all-optical neuromorphic systems.

5. Results and proof

5.1. Multi-synapse integration and thermal crosstalk analysis

The proposed photonic crystal synapse has been meticulously

engineered to facilitate the integration of multiple synapses while minimizing electromagnetic field interference. Numerical simulations of the electric and magnetic field distributions at a wavelength of 1504 nm demonstrate that the field intensities at the structure edges, located approximately 4a from the central waveguide, are effectively negligible (Fig. 14). This characteristic guarantees that each synapse operates independently, without performance perturbation from adjacent synapses.

To evaluate the effect of thermal crosstalk during the PCM phase-change process, the thermal conductivities of the employed materials—including silicon, silicon dioxide, GST, and air—were carefully considered. Amorphous GST exhibits a thermal conductivity of 0.2–0.3 W/m·K, which increases to 0.4–0.6 W/m·K in the crystalline phase (Ríos et al., 2015; Le Gallo et al., 2016). In comparison, crystalline silicon has a much higher thermal conductivity of 148 W/m·K (Yamasue et al., 2002), while SiO₂ (1.4 W/m·K (Zhu et al., 2018) and air (0.026–0.076 W/m·K (Rodrigues et al., 2021) act as effective thermal insulators. These differences confine the heating region primarily within the GST element and the silicon cavity rod, thereby minimizing heat leakage to adjacent rods and neighboring synapses.

For clarity, Table 1 summarizes the optical and thermal parameters of all materials employed. This analysis demonstrates that, even under multi-synapse integration, neighboring synapses operate with minimal thermal interference and can be regarded as nearly independent units, ensuring the scalability of the proposed architecture.

Moreover, by carefully controlling the amplitude and duration of the optical excitation pulses, the phase-change process can be precisely regulated, preventing unintentional crystallization in nearby synapses. This behavior confirms that the proposed device is inherently robust against thermal crosstalk and well-suited for reliable multi-synapse integration.

Leveraging this design, scalable multi-synapse integration is achievable, as depicted in Fig. 15. Each synapse maintains autonomous operation, representing a clear advancement over previous architectures. This capability reinforces the potential of the proposed photonic crystal synaptic platform for deployment in complex optical neural networks, enabling system-level integration while preserving precise control over synaptic weight modulation and dynamic response.

5.2. Reliability and durability of GST-PCM in neuromorphic synapses

The proposed GST-PCM-based neuromorphic photonic synapse demonstrates high reliability and durability due to the careful design of

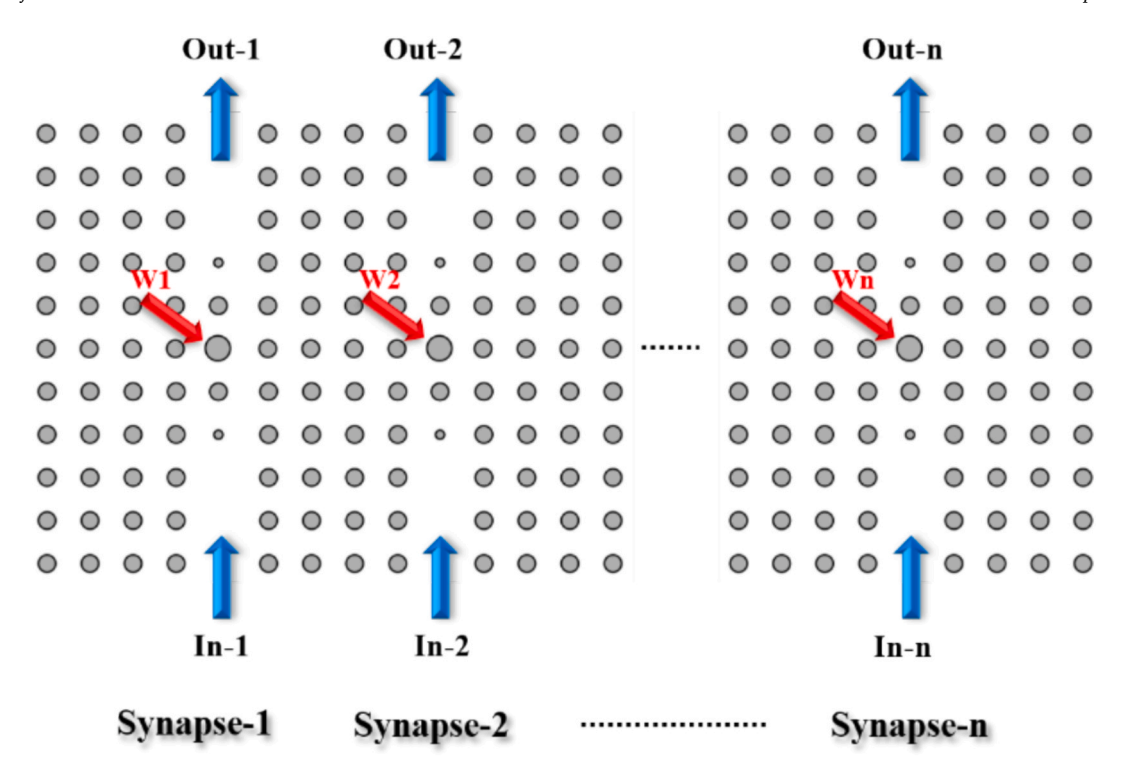


Fig. 15. Multi-synapse integration.

the phase-change material operation. In this structure, the GST-PCM element undergoes gradual modulation of its crystallization fraction rather than abrupt binary transitions between amorphous and crystalline states. This approach significantly reduces thermal stress and material fatigue, enhancing the endurance of the device.

Experimental studies on $Ge_2Sb_2Te_5$ have shown endurance typically ranging from 10^5 to 10^8 switching cycles, depending on the device configuration, pulse energy profile, and thermal management strategies, with optimized designs achieving up to 10^8 cycles (Wang et al., 2024; Ríos et al., 2015; Martin-Monier et al., 2022; Wang et al., 2020; Kim et al., 2019; Burr et al., 2008). In the proposed synapse, low-energy optical pulses with carefully controlled duration and amplitude enable precise tuning of crystallinity while minimizing unwanted thermal accumulation.

Furthermore, the GST-PCM element is thermally confined within a silicon rod and an air substrate with low thermal conductivity. This confinement localizes heat and prevents thermal diffusion to adjacent regions, ensuring that the applied energy efficiently drives the phase transition with minimal thermal leakage.

These design strategies collectively provide enhanced long-term reliability and stability of the proposed optical synapse under repeated operation, making the structure suitable for robust implementation in optical neuromorphic computing systems.

5.3. Parametric analysis of structural variations

A comprehensive parametric study was conducted to examine the effects of variations in the central rod radius (r_c) , scattering rods radii (r_s) , and lattice constant on the optical performance of the proposed photonic crystal synapse. The results, shown in Fig. 16, provide a detailed understanding of the sensitivity of synaptic transmission to structural parameters and demonstrate the robustness of the device under practical fabrication tolerances.

Eqs. (17–26) present the theoretical relationships and governing physical and thermal equations that describe the evolution of the GST-PCM temperature as a function of time and the applied laser power (Lizama et al., 2022; Saemathong et al., 2023; Bounouar et al., 2016;

Balanis, 2012; Consoli et al., 2020; Savini and Turowski, 2012). These equations, based on the physical principles and thermal properties of GST-PCM, provide a comprehensive model of the crystallization process and enable analysis of the effect of varying irradiation conditions on the optical properties and crystallization ratio of GST-PCM. A comparison of the simulated results with the theoretical predictions obtained from these equations validated the accuracy and reliability of the numerical circulations.

$$\rho c_{p} \frac{\partial T}{\partial t} + \rho c_{p} U.\nabla T = \nabla.(K\nabla T) + Q_{e}; \text{ Heat} - \text{Transfer Equation} \tag{17}$$

where ρ , c_p and K represent the density, specific heat capacity, and thermal conductivity of the GST-PCM, respectively.

$$Q_e = \frac{1}{2} Re(J.E^*) \tag{18}$$

$$J = \sigma E \tag{19}$$

$$\sigma = w\varepsilon_0\varepsilon_2 \tag{20}$$

$$\varepsilon_2 = 2nk \tag{21}$$

where n and k represent the real and imaginary parts of the GST-PCM refractive index, respectively.

$$E_{z_GST} = \sqrt{\frac{2I_{z_GST}}{C\varepsilon_0 n}} \tag{22}$$

where ε_0 is the permittivity of free space.

$$I_{z_GST} = (1 - R_{GST})I_{z_Si}e^{-\alpha_{GST}Z_{GST}}$$
 Beer –Lambert Law; (23)

$$I_{z=Si} = (1 - R_{Si})I_0e^{-\alpha_{Si}Z_{Si}} \text{ Beer - Lambert Law};$$
 (24)

R and α denote the reflection and absorption coefficients, respectively.

$$I_0 = \frac{P_0}{S} \tag{25}$$

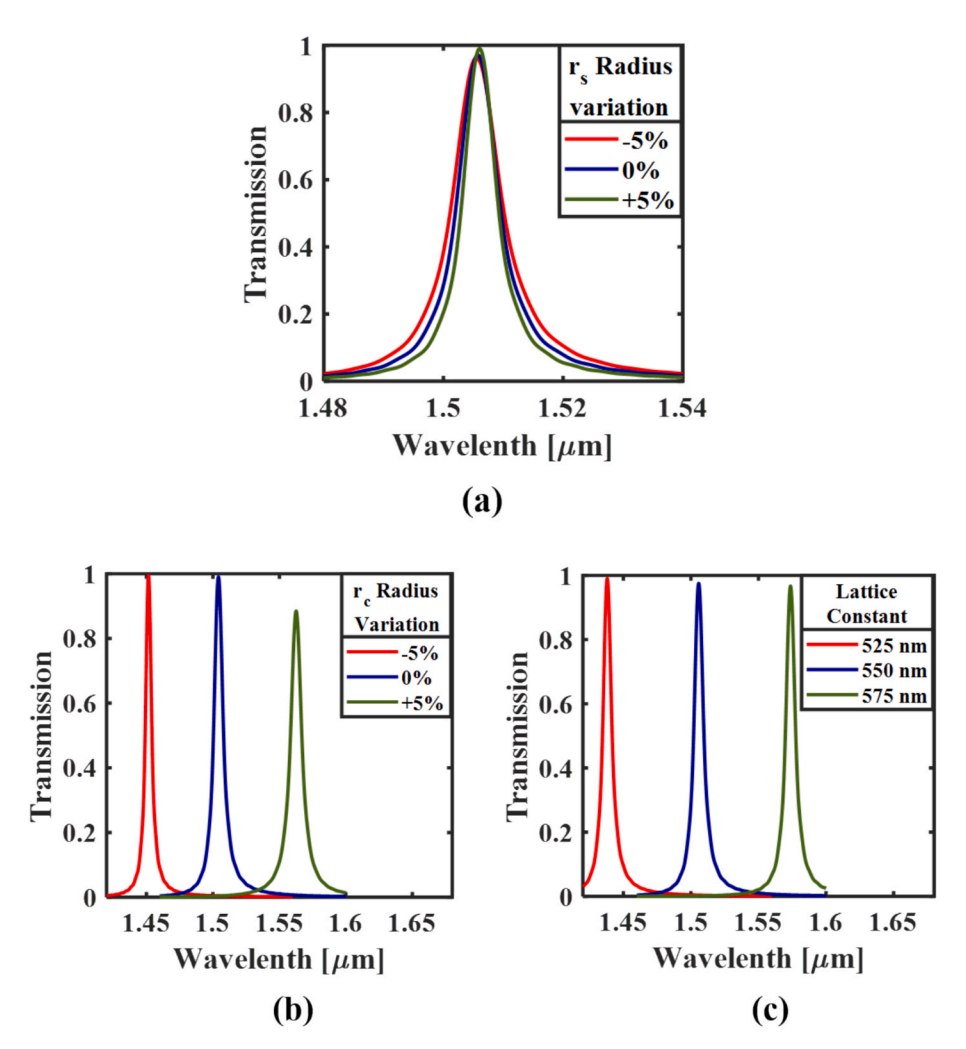


Fig. 16. Effect of variations in the (a) scattering rod radii (r_s) , (b) central rod radius (r_c) , and (c) lattice constant on the optical transmission of the proposed photonic crystal synapse.

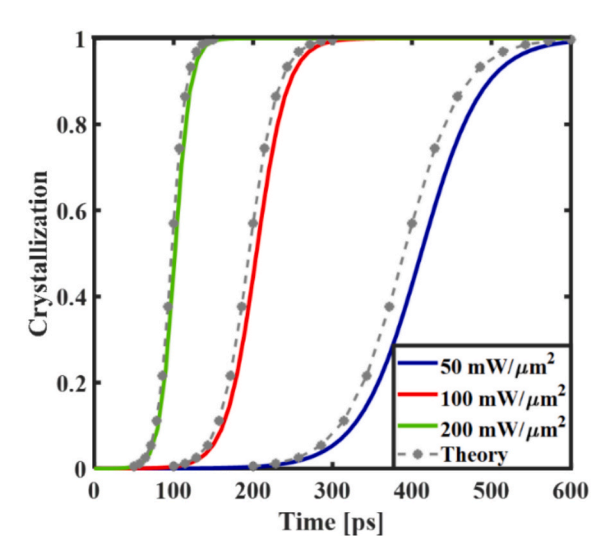


Fig. 17. GST-PCM crystallization fraction vs. laser pulse duration for different power densities of 50, 100, and 200 mW/ μ m². The results were obtained from numerical simulations using the finite element method. The dashed gray lines represent the theoretical calculations based on heat transfer equations. The good agreement between the simulation and theoretical results indicates the validity of the simulation model.

where S denotes the area of the synaptic structure, and P_0 denotes the laser power.

$$\alpha = \frac{4\pi k}{\lambda} \tag{26}$$

Fig. 17 illustrates the final crystallization ratio as a function of various weighting pulse powers (50, 100, and 200 mW/ μm^2) through FEM simulations and theoretical calculations (Eqs. (14–16)). The close alignment between the numerical simulation results and the theoretical models based on the discussed physical and thermal principles confirms the validity of the numerical simulation methods used in this study. As shown in the figure, the laser power applied to the proposed structure had an inverse relationship with the required crystallization time, indicating that increasing the laser power accelerated the crystallization process.

Reducing the energy consumption in the training process and adjusting the weight of neuromorphic synapses play a fundamental role in improving the efficiency, scalability, and operationalization of neuromorphic systems. In this study, we investigated the energy consumption of a single neuron consisting of the four proposed synapses. For this purpose, we used the gradient descent algorithm (Xie et al., 2023; Ruder, 2016) to adjust synaptic weights. This algorithm is optimal for neuromorphic models because of its efficient convergence and computational simplicity. Furthermore, the neuron activation function is defined as a sigmoid function ($f_z = 1/(1 + \exp(-z))$), providing a high

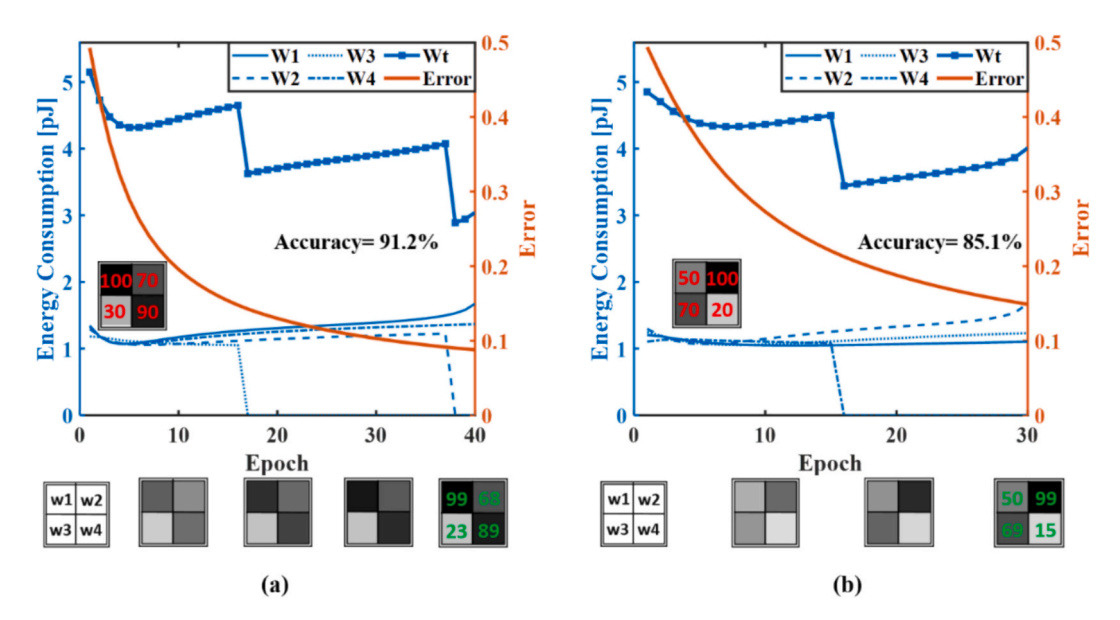


Fig. 18. Energy consumption and training error reduction in the weighting algorithm of an artificial neuron with four synapses using the gradient descent method for input patterns (a) [1_0.7_0.3_0.9], and (b) [0.5_1_0.7_0.2]. Red and green numbers in the patterns represent the target output and the trained neuron output, respectively. (For interpretation of the references to colour in this figure legend, the reader is referred to the web version of this article.)

Table 2Comparison of optoelectronic and artificial synaptic devices based on previous research.

Ref.	Structure	Active materials	Dimension [μm²]	Wavelength [nm]	Q-factor	Energy consumption	years
Li et al. (2016)	Bottom gate	IGZO/Al ₂ O ₃	20 × 40	365	_	13 pJ	2016
Cheng et al. (2017)	Tapered waveguide	Ge ₂ Sb ₂ Te ₅	36×14	_	_	~404 pJ	2017
Qin et al. (2017)	Bottom gate	Graphene/SWNTs	30×90	405/532	_	6 nJ	2017
Lee et al. (2017)	Two terminals	IGZO, ISZO, ISO, IZO	180×70	380-630	_	_	2017
Feldmann et al. (2017)	Crossing waveguide	Ge ₂ Sb ₂ Te ₅	30×30	1550	_	10 pJ	2017
Zheng et al. (2018)	Micro ring resonator	Ge ₂ Sb ₂ Te ₅	72×55	~1550	~7700	~620 pJ	2018
Wu et al. (2018)	Bottom gate	IGZO	10×100	254	_	0.6 nJ	2018
Yang et al. (2018)	Bottom gate	GZO/chitosan	80×1000	_	_	_	2018
Dai et al. (2018)	Bottom gate	C8-BTBT	200×6000	360	_	42 nJ	2018
Tan et al. (2018)	Two-terminal	SiNCs	2000×2000	UV-VisNIR	_	0.7 pJ	2018
John et al. (2018)	Multi-gate	MoS_2	9×20	445	~20	4.8 pJ	2018
Wang et al. (2018)	Bottom gate	CsPbBr ₃ QDs/pentacene	50×1000	UV-Vis.	~26	1.4 nJ	2018
Sun et al. (2018)	Lateral gate	IGZO/alkylated graphene oxide	10×10	405	-	362 pJ	2018
Liu et al. (2018)	Bottom gate	IZO	30×100	470	_	~ 35 nJ	2019
Zhang et al. (2019)	Micro ring resonator	Ge ₂ Sb ₂ Se ₄ Te ₁	590 × 380	1565	~24000	~ 5.5 μJ	2019
Shao et al. (2019)	Bottom gate	SWCNT	20×1000	520/940/1310		2.5 nJ	2019
Yin et al. (2019)	Bottom gate	SiNCs	10×120	UV-VisNIR		0.14 nJ	2019
Feldmann et al. (2019)	Waveguide	Ge ₂ Sb ₂ Te ₅	1530×120	1553.4	~1140	~710 pJ	2019
Wang et al (2019)	Bottom gate	CsPbBr ₃ QDs /PQT-12	30×1000	500	-	0.65 nJ	2019
Alguraishi et al. (2019)	lateral gate	In2O3	80×1600	365		~ 40 nJ	2019
Wang et al. (2019)	Bottom gate	MoS ₂ /PTCDA	2×5.3	532	_	10 pJ	2019
Pradhan et al. (2020)	graphene lattice	MAPbBr ₃		440		36.75 pJ	2020
Zhang et al. (2021)	Slot-ridge waveguides	Ge ₂ Sb ₂ Te ₅	2×10.5	1550	_	•	2021
Zhang et al. (2021)	directional coupler	Ge ₂ Sb ₂ Te ₅	2.8×15.8	1550	_	- ∼ 15pj	2021
Li et al. (2021)	Silicon Nanowires	Si NW	15×11	~550	_	1 nj	2021
Li et al. (2022)	Micro ring resonator	In ₂ Se ₃	25×17	1574	4800	~250 pJ	2022
Brückerhoff-Plückelmann et al. (2023)	Multi-mode interference	Ge ₂ Sb ₂ Te ₅	115×66	~1550		400 pJ	2023
Nohoji et al. (2024)	Photonic crystal	Ge ₂ Sb ₂ Te ₅	5.4×5.4	1310	900	_	2024
Morcillo et al. (2024)	meander-shaped	VO ₂ /Si	1.2×2.7	1550		- 1 nJ	2024
Laprais et al. (2024)	Thin Film	Sb ₂ s ₃	_	532	_	210 μJ	2024
Nohoji et al. (2025)	RR-MZI	Ge ₂ Sb ₂ Te ₅	10.5×20.2	1550	3226	_	2025
Nohoji et al. (2025)	DC-MZI	Ge ₂ Sb ₂ Se ₄ Te ₁	14.4×13.6	1320	360	_	2025
Nohoji et al. (2025)	Slab	Ge ₂ Sb ₂ Te ₅	2.97×2.57	1518	353	- 267 pj	2025
This Work	triangular Photonic crystal	$Ge_2Sb_2Te_5$	4.4 × 3.3	1504	195	~1.5 pJ	_

degree of flexibility in the learning process owing to its nonlinear characteristics. The energy consumption in each epoch was calculated using Eq. (27) (Wang et al., 2021):

$$dE = I_0 \times S \times dt \tag{27}$$

where dE is the energy consumption and S, I_0 , and dt are the area of the

synapse structure for the irradiated laser, the power density, and the pulse duration of the irradiated laser for weight adjustment,

We set the laser power density to 100 mW/ μ m² for tuning synaptic weights and trained the proposed synaptic weights, W1 to W4, using a supervised learning method.

The energy consumption and learning error variations for the two patterns are presented in Fig. 18 as functions of the number of algorithm iterations. The results demonstrate that the energy consumption of each synapse per epoch is less than 1.5 pJ, indicating the remarkable efficiency of the proposed structure. Furthermore, the learning process demonstrated effective error reduction and optimal convergence within a few iterations, validating the ability of the structure to handle complex learning tasks.

Table 2 presents a comparative analysis of optoelectronic synaptic devices and artificial synaptic structures. This comparison includes key features, such as structure, active materials, dimensions, quality-factor, stimulation wavelength, and energy consumption.

Table 2 provides a detailed comparison of the proposed photonic crystal synapse with previous optoelectronic and artificial synaptic devices. This comparison highlights several distinctive advantages of the present design, including its compact footprint $(4.4 \times 3.3 \mu m^2)$ for efficient integration into photonic circuits, low energy consumption (~1.5 pJ per synaptic operation), and high cascadability, which enables the construction of larger-scale optical neural networks.

Using GST-PCM as an active material contributes to better performance of photonic crystal structures. These characteristics make our device a promising candidate for low-power, high-performance optoelectronic synaptic applications.

6. Fabrication method

To fabricate the proposed photonic crystal structure, silicon dioxide (SiO₂) and silicon (Si) layers are deposited on a fused silica substrate with thicknesses of 1.5a and 1.1a, respectively. This process is performed using techniques such as chemical vapor deposition (CVD) or physical vapor deposition (PVD) (Fujisaki et al., 2015). Precise control of the thickness and uniformity of these layers is essential to achieve the desired dimensions in the final structure.

Next, a thin layer of photoresist, such as polymethyl methacrylate (PMMA), is uniformly deposited on the silicon surface. Using electron beam lithography (EBL), a precise pattern is designed and executed to create a central hole in the silicon structure with a hole diameter of 130 nm.

After EBL patterning, plasma etching or reactive ion etching (RIE) is used to etch the hole. This etching process is fine-tuned to achieve a hole depth of 700 nm at the center of the silicon structure. Subsequently, a phase change material (GST-PCM) composed of germanium, selenium, and tellurium is locally deposited into the etched hole via atomic layer deposition (ALD) (Guo et al., 2019; Eom et al., 2012). Precise control of the thickness (200 nm) and proper placement of the GST-PCM material inside the hole are essential to ensure optimal optical properties of the photonic crystal.

After GST-PCM deposition, a silicon layer is deposited inside the silicon hole and on top of the GST-PCM material using plasma-enhanced chemical vapor deposition (PECVD). To remove residual photoresist (PMMA), the structure is immersed in an acetone solution at room temperature, rinsed with isopropanol (IPA), and then dried with nitrogen gas. In the following step, a new pattern for photonic crystal rods is designed using electron beam lithography (EBL). A new thin layer of PMMA is applied to the silicon surface and evenly distributed via spincoating. Subsequently, another etching step is performed to remove the unwanted silicon regions. This is achieved using reactive ion etching or plasma etching, utilizing gases such as sulfur hexafluoride (SF₆) or chlorine (Cl₂), which are specifically designed for silicon etching. The etching process is carefully controlled to ensure that only the predefined

regions are etched away, leaving silicon rods with the desired dimensions. Finally, a photonic crystal structure with desired properties is formed.

7. Conclusion

In this study, an all-optical neuromorphic synaptic structure based on photonic crystals, equipped with GST-PCM, was designed and analyzed. Simulation results using accurate FDTD and FEM methods demonstrated that the proposed structure can achieve a transmission efficiency exceeding 99 % and a reflection reduction of less than -20 dB at a wavelength of 1504 nm. The ability to precisely control the synaptic weights using focused laser irradiation makes this structure a promising candidate for implementing optical artificial neural networks.

The proposed design leverages the exceptional properties of photonic crystals to achieve precise optical control, extremely compact dimensions, and ultra-low power consumption. This design is advantageous for optical neural networks and processing systems where high density and energy efficiency are critical.

The design performance parameters, including the Q-factor and FWHM, were optimized by varying the radius and thickness of the photonic crystal rods, which improved the optical efficiency.

The proposed structure can accelerate synaptic weights through controlled laser pulse irradiation and optimize the learning processes in neuromorphic systems, leading to significant progress towards realizing all-optical processing systems.

Overall, the proposed design represents a significant step towards the development of all-optical neuromorphic computing. Its low power consumption, compact size, and high speed make it a promising candidate for application in optical artificial intelligence, integrated neural networks, and optical neuromorphic systems. This design represents an advanced and efficient platform for the next generation of optical computing and processing, which could significantly contribute to the advancement of new technologies in this field.

CRediT authorship contribution statement

Amir Hossein Abdollahi Nohoji: Writing - original draft, Visualization, Validation, Software, Methodology, Investigation, Formal analysis, Conceptualization. Parviz Keshavarzi: Validation, Supervision, Conceptualization. Mohammad Danaie: Writing - review & editing, Validation. Supervision, Investigation, Formal analysis, Conceptualization.

Declaration of competing interest

The authors declare that they have no known competing financial interests or personal relationships that could have appeared to influence the work reported in this paper.

Data availability

Data will be made available on request.

References

Akahane, Y., Asano, T., Song, B.-S., Noda, S., 2005. Fine-tuned high-Q photonic-crystal nanocavity, Opt. Express 13, 1202-1214.

Alkhamisi, M.M., Marzouk, S.Y., Wassel, A.R., El-Mahalawy, A.M., Almotiri, R.A., 2022. Multi-functional platform based on amorphous Ge2Sb2Te5 thin films for photo/ thermodetection and non-volatile memory applications. Mater. Sci. Semicond. Process, 149, 106856.

Alquraishi, W., Fu, Y., Qiu, W., Wang, J., Chen, Y., Kong, L.-A., Sun, J., Gao, Y., 2019. Hybrid optoelectronic synaptic functionality realized with ion gel-modulated In2O3 phototransistors. Org. Electron. 71, 72-78.

Asgari, S., Fabritius, T., 2020. Tunable mid-infrared graphene plasmonic cross-shaped

resonator for demultiplexing application. Appl. Sci. 10, 1193.

Aspnes, D.E., Studna, A.A., 1983. Dielectric functions and optical parameters of si, ge, gap, gaas, gasb, inp, inas, and insb from 1.5 to 6.0 ev. Phys. Rev. B 27, 985.

- Auer, P., Burgsteiner, H., Maass, W., 2008. A learning rule for very simple universal approximators consisting of a single layer of perceptrons. Neural networks 21, 786–795.
- Bakan, G., Gerislioglu, B., Dirisaglik, F., Jurado, Z., Sullivan, L., Dana, A., Lam, C., Gokirmak, A., Silva, H., 2016. Extracting the temperature distribution on a phasechange memory cell during crystallization. J. Appl. Phys. 120.
- Balanis, C.A., 2012. Advanced Engineering Electromagnetics. John Wiley & Sons.
 Bednarkiewicz, A., Szalkowski, M., Majak, M., Korczak, Z., Misiak, M., Maćkowski, S.,
 2023. All-optical data processing with photon-avalanching nanocrystalline photonic synapse. Adv. Mater. 35, 2304390.
- Bounouar, A., Gueraoui, K., Taibi, M., Lahlou, A., Driouich, M., Sammouda, M., Men-La-Yakhaf, S., Belcadi, M., 2016. Numerical and mathematical modeling of unsteady heat transfer within a spherical cavity: Applications laser in medicine. Contemp. Eng. Sci. 9, 1183–1199.
- Brückerhoff-Plückelmann, F., Feldmann, J., Wright, C.D., Bhaskaran, H., Pernice, W.H. P., 2021. Chalcogenide phase-change devices for neuromorphic photonic computing. J. Appl. Phys. 129.
- Brückerhoff-Plückelmann, F., Bente, I., Becker, M., Vollmar, N., Farmakidis, N., Lomonte, E., Lenzini, F., Wright, C.D., Bhaskaran, H., Salinga, M., et al., 2023. Event-driven adaptive optical neural network. Sci. Adv. 9, eadi9127.
- Burr, G.W., Kurdi, B.N., Scott, J.C., Lam, C.H., Gopalakrishnan, K., Shenoy, R.S., 2008. Overview of candidate device technologies for storage-class memory. IBM J. Res. Dev. 52. 449–464.
- Burr, G.W., Shelby, R.M., Sebastian, A., Kim, S., Kim, S., Sidler, S., Virwani, K., Ishii, M., Narayanan, P., Fumarola, A., 2017. Neuromorphic computing using non-volatile memory. Adv. Phys. X 2, 89–124.
- Cao, T., Wang, R., Simpson, R.E., Li, G., 2020. Photonic Ge-Sb-Te phase change metamaterials and their applications. Prog. Quantum Electron. 74, 100299.
- Chakraborty, I., Saha, G., Sengupta, A., Roy, K., 2018. Toward fast neural computing using all-photonic phase change spiking neurons. Sci. Rep. 8, 12980.
- Chakraborty, I., Saha, G., Roy, K., 2019. Photonic in-memory computing primitive for spiking neural networks using phase-change materials. Phys. Rev. Appl. 11, 14063.
- Chakraverty, S., Sahoo, D.M., Mahato, N.R., Chakraverty, S., Sahoo, D.M., Mahato, N.R., 2019. Delta learning rule and backpropagation rule for multilayer perceptron. Concepts Soft Comput Fuzzy ANN with Program. 189–195.
- Cheng, Z., R'ios, C., Pernice, W.H.P., Wright, C.D., Bhaskaran, H., 2017. On-chip photonic synapse. Sci. Adv. 3, e1700160.
- Consoli, F., Tikhonchuk, V.T., Bardon, M., Bradford, P., Carroll, D.C., Cikhardt, J., Cipriani, M., Clarke, R.J., Cowan, T.E., Danson, C.N., 2020. Laser produced electromagnetic pulses: generation, detection and mitigation. High Power Laser Sci. Eng. 8, e22.
- Dai, S., Wu, X., Liu, D., Chu, Y., Wang, K., Yang, B., Huang, J., 2018. Light-stimulated synaptic devices utilizing interfacial effect of organic field-effect transistors. ACS Appl. Mater. Interfaces 10, 21472–21480.
- Dhingra, N., Song, J., Saxena, G.J., Sharma, E.K., Rahman, B.M.A., 2019. Design of a compact low-loss phase shifter based on optical phase change material. IEEE Photon. Technol. Lett. 31, 1757–1760.
- Du, Q., 2022. In: Phase Change Materials, in Emergent Micro-and Nanomaterials for Optical, Infrared, and Terahertz Applications. CRC Press, pp. 239–259.
- Du, K.-L., Leung, C.-S., Mow, W.H., Swamy, M.N.S., 2022. Perceptron: Learning, generalization, model selection, fault tolerance, and role in the deep learning era. Mathematics 10, 4730.
- Dubey, S.R., Singh, S.K., Chaudhuri, B.B., 2022. Activation functions in deep learning: A comprehensive survey and benchmark. Neurocomputing 503, 92–108.
- Elliott, S.R., 2015. Chalcogenide Phase-Change Materials: Past and Future. Int. J. Appl. Glas. Sci. 6, 15–18.
- Eom, T., Choi, S., Choi, B.J., Lee, M.H., Gwon, T., Rha, S.H., Lee, W., Kim, M.-S., Xiao, M., Buchanan, I., 2012. Conformal formation of (GeTe2)(1–x)(Sb2Te3) x layers by atomic layer deposition for nanoscale phase change memories. Chem. Mater. 24, 2099–2110.
- Feldmann, J., Stegmaier, M., Gruhler, N., R'ios, C., Bhaskaran, H., Wright, C.D., Pernice, W.H.P., 2017. Calculating with light using a chip-scale all-optical abacus. Nat. Commun. 8, 1256.
- Feldmann, J., Youngblood, N., Wright, C.D., Bhaskaran, H., Pernice, W.H.P., 2019. All-optical spiking neurosynaptic networks with self-learning capabilities. Nature 569, 208–214.
- Fu, T., Zhang, J., Sun, R., Huang, Y., Xu, W., Yang, S., Zhu, Z., Chen, H., 2024. Optical neural networks: progress and challenges. Light Sci. Appl. 13, 263.
- Fujisaki, Y., Sasago, Y., Kobayashi, T., 2015. Amorphous thin GeSbTe phase-change films prepared by radical-assisted metal-organic chemical vapor deposition. Thin Solid Films 583, 55–59.
- Gerislioglu, B., Bakan, G., Ahuja, R., Adam, J., Mishra, Y.K., Ahmadivand, A., 2020. The role of Ge2Sb2Te5 in enhancing the performance of functional plasmonic devices. Mater. Today Phys. 12, 100178.
- Gnawali, R., Volk, A., Hendrickson, J.R., Vangala, S., Banerjee, P.P., 2024. Tunable fast optical filter using metamaterials and phase change material. in Metamaterials XIV, SPIE, Vol. 12990, p. 1299002.
- Guo, P., Sarangan, A.M., Agha, I., 2019. A review of germanium-antimony-telluride phase change materials for non-volatile memories and optical modulators. Appl. Sci. 9, 530.
- Guo, X., Xiang, J., Zhang, Y., Su, Y., 2021. Integrated neuromorphic photonics: synapses, neurons, and neural networks. Adv. Photonics Res. 2, 2000212.
- Henseler, J., 2005. Back propagation. Artif. Neural Networks An Introd. to ANN Theory Pract. 37-66.
- Hong, P., Liu, J., Qin, K., Tian, R., Peng, L., Su, Y., Gan, Z., Yu, X., Ye, L., Zhu, M., 2024. Towards optical information recording: A robust visible-light-driven molecular

- photoswitch with the ring-closure reaction yield exceeding 96.3%. Angew. Chemie Int. Ed. 63, e202316706.
- Huo, Z., Sun, Q., Yu, J., Wei, Y., Wang, Y., Cho, J.H., Wang, Z.L., 2025. Neuromorphic devices assisted by machine learning algorithms. Int. J. Extrem. Manuf.
- Hurtado, A., Romeira, B., Buckley, S., Cheng, Z., Shastri, B.J., 2022. Emerging optical materials, devices and systems for photonic neuromorphic computing: Introduction to special issue. Opt. Mater. Express 12, 4328–4331.
- Huynh, P.K., Varshika, M.L., Paul, A., Isik, M., Balaji, A., Das, A., 2022. Implementing spiking neural networks on neuromorphic architectures: A review. arXiv Prepr arXiv2202.08897.
- Jauro, F., Chiroma, H., Gital, A.Y., Almutairi, M., Shafi'i, M.A., Abawajy, J.H., 2020. Deep learning architectures in emerging cloud computing architectures: Recent development, challenges and next research trend. Appl. Soft Comput. 96, 106582.
- John, R.A., Liu, F., Chien, N.A., Kulkarni, M.R., Zhu, C., Fu, Q., Basu, A., Liu, Z., Mathews, N., 2018. Synergistic gating of electro-iono-photoactive 2D chalcogenide neuristors: Coexistence of hebbian and homeostatic synaptic metaplasticity. Adv. Mater. 30, 1800220.
- Julian, M.N., Williams, C., Borg, S., Bartram, S., Kim, H.J., 2020. Reversible optical tuning of GeSbTe phase-change metasurface spectral filters for mid-wave infrared imaging. Optica 7, 746–754.
- Karlik, B., Olgac, A.V., 2011. Performance analysis of various activation functions in generalized MLP architectures of neural networks. Int. J. Artif. Intell. Expert Syst. 1, 111–122.
- Kim, S., Burr, G.W., Kim, W., Nam, S.-W., 2019. Phase-change memory cycling endurance. MRS Bull. 44, 710–714.
- Kiselev, A.V., Ionin, V.V., Burtsev, A.A., Eliseev, N.N., Mikhalevsky, V.A., Arkharova, N. A., Khmelenin, D.N., Lotin, A.A., 2022. Dynamics of reversible optical properties switching of Ge2Sb2Te5 thin films at laser-induced phase transitions. Opt. Laser Technol. 147, 107701.
- Kumar, S., Sharma, V., 2020. Improvement in stability of GST PCMs on Sm addition for memory devices. J. Non. Cryst. Solids 532, 119887.
- Kunkel, T., Vorobyov, Y., Smayev, M., Lazarenko, P., Romashkin, A., Kozyukhin, S., 2022. Crystallization of GST225 thin film induced by a single femtosecond laser pulse: Experimental and theoretical study. Mater. Sci. Semicond. Process. 139, 106350.
- Laporte, F., Katumba, A., Dambre, J., Bienstman, P., 2018. Numerical demonstration of neuromorphic computing with photonic crystal cavities. Opt. Express 26, 7955–7964.
- Laprais, C., Zrounba, C., Bouvier, J., Blanchard, N., Bugnet, M., Gassenq, A., Gutiérrez, Y., Vazquez-Miranda, S., Espinoza, S., Thiesen, P., 2024. Reversible singlepulse laser-induced phase change of Sb2S3 thin films: Multi-physics modeling and experimental demonstrations. Adv. Opt. Mater. 12, 2401214.
- Le Gallo, M., Athmanathan, A., Krebs, D., Sebastian, A., 2016. Evidence for thermally assisted threshold switching behavior in nanoscale phase-change memory cells. J. Appl. Phys. 119.
- Lee, M., Lee, W., Choi, S., Jo, J.-W., Kim, J., Park, S.K., Kim, Y.-H., 2017. Brain-inspired photonic neuromorphic devices using photodynamic amorphous oxide semiconductors and their persistent photoconductivity. Adv. Mater. 29, 1700951.
- Li, H.K., Chen, T.P., Liu, P., Hu, S.G., Liu, Y., Zhang, Q., Lee, P.S., 2016. A light-stimulated synaptic transistor with synaptic plasticity and memory functions based on InGaZnOx–Al2O3 thin film structure. J. Appl. Phys. 119.
- Li, Q., Wang, T., Su, Y., Yan, M., Qiu, M., 2010. Coupled mode theory analysis of mode-splitting in coupled cavity system. Opt. Express 18, 8367–8382.
 Li, T., Wang, Y., Li, W., Mao, D., Benmore, C.J., Evangelista, I., Xing, H., Li, Q., Wang, F.,
- Li, T., Wang, Y., Li, W., Mao, D., Benmore, C.J., Evangelista, I., Xing, H., Li, Q., Wang, F., Sivaraman, G., et al., 2022. Structural phase transitions between layered indium selenide for integrated photonic memory. Adv Mater. 34, 2108261.
- Li, X., Yu, B., Wang, B., Bi, R., Li, H., Tu, K., Chen, G., Li, Z., Huang, R., Li, M., 2021. Complementary photo-synapses based on light-stimulated porphyrin-coated silicon nanowires field-effect transistors (LPSNFET). Small 17, 2101434.
- Li, Y., Zhang, Y., Cheng, S., Li, X., Feng, Y., Jin, W., Liu, Z., Qin, Y., Yuan, L., 2024. All-fiber synapse based on Ge 2 Sb 2 Te 5 for reconfigurable logic operations. J. Light, Technol.
- Liu, Y., Huang, W., Wang, X., Liang, R., Wang, J., Yu, B., Ren, T.-L., Xu, J., 2018.
 A hybrid phototransistor neuromorphic synapse. IEEE J. Electron Devices Soc. 7, 12, 17
- Lizama, C., Murillo Arcila, M., Trujillo Guillen, M., 2022. Fractional Beer-Lambert law in laser heating of biological tissue. AIMS Math. 14, 14444–14459.
- Lu, Y., Yan, X., 2024. Ultra-high optical contrast of the plasmonic memory based on Fabry-Perot cavity and phase change materials.
- Lu, W., Chen, Q., Zeng, H., Wang, H., Liu, L., Guo, T., Chen, H., Wang, R., 2023. All optical artificial synapses based on long-afterglow material for optical neural network. Nano Res. 16, 10004–10010.
- Luo, T., Wong, W.-F., Goh, R.S.M., Do, A.T., Chen, Z., Li, H., Jiang, W., Yau, W., 2023. Achieving green ai with energy-efficient deep learning using neuromorphic computing. Commun. ACM 66, 52–57.
- Ma, B., Zhang, P., Wang, H., Zhang, T., Zeng, J., Zhang, Q., Wang, G., Xu, P., Zhang, W., Dai, S., 2016. Photonic-crystal switch divider based on Ge2Sb2Te5 thin films. Appl. Opt. 55, 9205–9210.
- Mahata, C., Park, J., Ismail, M., Kim, S., 2023. Demonstration of electronic and optical synaptic properties modulation of reactively sputtered zinc-oxide-based artificial synapses. J. Alloys Compd. 938, 168539.
- Malitson, I.H., 1965. Interspecimen comparison of the refractive index of fused silica. J. Opt. Soc. Am. 55, 1205–1209.
- Martin-Monier, L., Popescu, C.C., Ranno, L., Mills, B., Geiger, S., Callahan, D., Moebius, M., Hu, J., 2022. Endurance of chalcogenide optical phase change materials: A review. Opt. Mater. Express 12, 2145–2167.

- Mondal, S., 2008. Phase change materials for smart textiles—An overview. Appl. Therm. Eng. 28, 1536–1550.
- Morcillo, J.-F., Sanchis, P., Parra, J., 2024. On-chip electro-optical spiking VO2/Si device with an inhibitory leaky integrate-and-fire response. Opt. Mater. Express 14, 2681–2693.
- Nohoji, A.H.A., Danaie, M., 2022. Highly sensitive refractive index sensor based on photonic crystal ring resonators nested in a Mach-Zehnder interferometer. Opt. Quantum Electron. 54, 574.
- Nohoji, A.H.A., Keshavarzi, P., Danaie, M., 2024. A photonic crystal waveguide intersection using phase change material for optical neuromorphic synapses. Opt. Mater. (Amst) 151, 115372.
- Nohoji, A.H.A., Keshavarzi, P., Danaie, M., 2025. High Q-factor ring resonator nested in Mach–Zehnder interferometer based on Ge2Sb2Te5 phase change material for realization of synapses in optical neural networks. Phys. Scr. 100, 65515.
- Nohoji, A.H.A., Keshavarzi, P., Danaie, M., 2025. Silicon-based all-optical photonic crystal neuromorphic synapses using Ge2Sb2Te5. Opt. Contin. 4, 1591–1609.
- Nohoji, A.H.A., Keshavarzi, P., Danaie, M., 2025. High-performance all-optical photonic crystal synapse based on Mach-Zehnder interferometer and directional coupler utilizing GSST phase-change material. Results Phys. 108338.
- Pernice, W.H.P., Bhaskaran, H., 2012. Photonic non-volatile memories using phase change materials. Appl. Phys. Lett. 101.
- Pourmand, M., Choudhury, P.K., 2022. Programmable phase-change medium-assisted hyperbolic metamaterial as a dual-band nearly perfect absorber. JOSA B 39, 1222–1228.
- Pradhan, B., Das, S., Li, J., Chowdhury, F., Cherusseri, J., Pandey, D., Dev, D., Krishnaprasad, A., Barrios, E., Towers, A., 2020. Ultrasensitive and ultrathin phototransistors and photonic synapses using perovskite quantum dots grown from graphene lattice. Sci. Adv. 6, eaay5225.
- Prakash, M., Murphy, J., St Laurent, R., Friedman, N., Crespo, E.L., Bjorefeldt, A., Pal, A., Bhagat, Y., Kauer, J.A., Shaner, N.C., 2022. Selective control of synapticallyconnected circuit elements by all-optical synapses. Commun. Biol. 5, 33.
- Qin, S., Wang, F., Liu, Y., Wan, Q., Wang, X., Xu, Y., Shi, Y., Wang, X., Zhang, R., 2017. A light-stimulated synaptic device based on graphene hybrid phototransistor. 2D Mater. 4, 35022.
- Qu, Y., Li, Q., Cai, L., Pan, M., Ghosh, P., Du, K., Qiu, M., 2018. Thermal camouflage based on the phase-changing material GST. Light Sci. Appl. 7, 26
- Ramchoun, H., Ghanou, Y., Ettaouil, M., Janati Idrissi, M.A., 2016. Multilayer perceptron: Architecture optimization and training.
- Rashidi, A., Hatef, A., Entezar, S.R., 2021. Thermally induced tuning of absorption in a Ge2Sb2Te5-based one-dimensional Fibonacci quasicrystal. Opt. Laser Technol. 137, 106831.
- Rashidi, S., Rashidi, A., Entezar, S.R., 2023. Tunable NIR absorption in a Ge2Sb2Te5-based 1D asymmetric nonlinear hybrid nanostructure. Opt. Laser Technol. 157, 108664.
- Ríos, C., Stegmaier, M., Hosseini, P., Wang, D., Scherer, T., Wright, C.D., Bhaskaran, H., Pernice, W.H.P., 2015. Integrated all-photonic non-volatile multi-level memory. Nat. Photonics 9, 725–732.
- Rodrigues, F.M., Moreno Júnior, A.L., Munaiar Neto, J., 2021. Short columns composed of concrete-filled steel tubes in a fire situation–Numerical model and the "air-gap" effect. Rev. IBRACON Estruturas e Mater. 15, e15309.
- Rodriguez-Hernandez, G., Hosseini, P., Ríos, C., Wright, C.D., Bhaskaran, H., 2017.
 Mixed-mode electro-optical operation of Ge2Sb2Te5 nanoscale crossbar devices.
 Adv. Electron. Mater. 3. 1700079.
- Ruder, S., 2016. An overview of gradient descent optimization algorithms. arXiv Prepr. arXiv1609.04747.
- Saemathong, J., Pannucharoenwong, N., Mongko, V., Vongpradubchai, S., Rattanadecho, P., 2023. Analyzing two laser thermal energy calculation equations: A comparison of Beer-Lambert's law and light transport equation. Eng. Sci. 24, 912.
- Savini, A., Turowski, J., 2012. Electromagnetic Fields in Electrical Engineering. Springer Science & Business Media.
- Schuman, C.D., Kulkarni, S.R., Parsa, M., Mitchell, J.P., Date, P., Kay, B., 2022. Opportunities for neuromorphic computing algorithms and applications. Nat. Comput. Sci. 2, 10–19.
- Shao, L., Wang, H., Yang, Y., He, Y., Tang, Y., Fang, H., Zhao, J., Xiao, H., Liang, K., Wei, M., et al., 2019. Optoelectronic properties of printed photogating carbon nanotube thin film transistors and their application for light-stimulated neuromorphic devices. ACS Appl. Mater. & interfaces 11, 12161–12169.
- Song, S., Kim, J., Kwon, S.M., Jo, J., Park, S.K., Kim, Y., 2021. Recent progress of optoelectronic and all-optical neuromorphic devices: a comprehensive review of device structures, materials, and applications. Adv. Intell. Syst. 3, 2000119.
- Stegmaier, M., Ríos, C., Bhaskaran, H., Wright, C.D., Pernice, W.H.P., 2017. Nonvolatile all-optical 1×2 switch for chipscale photonic networks. Adv. Opt. Mater. 5, 1600346.
- Sun, J., Oh, S., Choi, Y., Seo, S., Oh, M.J., Lee, M., Lee, W.B., Yoo, P.J., Cho, J.H., Park, J., 2018. Optoelectronic synapse based on igzo-alkylated graphene oxide hybrid structure. Adv. Funct. Mater. 28, 1804397.
- Tan, H., Ni, Z., Peng, W., Du, S., Liu, X., Zhao, S., Li, W., Ye, Z., Xu, M., Xu, Y., et al., 2018. Broadband optoelectronic synaptic devices based on silicon nanocrystals for neuromorphic computing. Nano Energy 52, 422–430.
- Tang, J., Yuan, F., Shen, X., Wang, Z., Rao, M., He, Y., Sun, Y., Li, X., Zhang, W., Li, Y., 2019. Bridging biological and artificial neural networks with emerging neuromorphic devices: fundamentals, progress, and challenges. Adv. Mater. 31, 1902761.
- Tao, W., Wu, Y., Zhao, F., Li, C., Fang, B., Jing, X., Yu, M., 2024. Research progress in metamaterials and metasurfaces based on the phase change material Ge2Sb2Te5. Opt. Laser Technol. 177, 111064.

Wang, S., Chen, C., Yu, Z., He, Y., Chen, X., Wan, Q., Shi, Y., Zhang, D.W., Zhou, H., Wang, X., 2019. A MoS2/PTCDA hybrid heterojunction synapse with efficient photoelectric dual modulation and versatility. Adv. Mater. 31, 1806227.

- Wang, K., Dai, S., Zhao, Y., Wang, Y., Liu, C., Huang, J., 2019. Light-stimulated synaptic transistors fabricated by a facile solution process based on inorganic perovskite quantum dots and organic semiconductors. Small 15, 1900010.
- Wang, C., Hu, Y., Zhu, X., 2024. Effect of ultraviolet radiation on properties of Ge2Sb2Te5 phase change films. Langmuir 40, 16936–16945.
- Wang, Y., Lv, Z., Chen, J., Wang, Z., Zhou, Y., Zhou, L., Chen, X., Han, S., 2018. Photonic synapses based on inorganic perovskite quantum dots for neuromorphic computing. Adv. Mater. 30, 1802883.
- Wang, R., Shen, J., Chen, X., Wang, H., Song, S., Song, Z., 2020. High thermal stability and fast operation speed phase-change memory devices containing Hf-doped Ge2Sb2Te5 films. Mater. Lett. 278, 128402.
- Wang, J., Xu, C., Zhang, J., Zhong, R., 2022. Big data analytics for intelligent manufacturing systems: A review. J. Manuf. Syst. 62, 738–752.
- Wang, Y., Yin, L., Huang, W., Li, Y., Huang, S., Zhu, Y., Yang, D., Pi, X., 2021. Optoelectronic synaptic devices for neuromorphic computing. Adv. Intell. Syst. 3, 2000099.
- Wang, D., Zhao, L., Yu, S., Shen, X., Wang, J.-J., Hu, C., Zhou, W., Zhang, W., 2023. Non-volatile tunable optics by design: from chalcogenide phase-change materials to device structures. Mater. Today 68, 334–355.
- Waoo, A.A., Soni, B.K., 2021. Performance analysis of sigmoid and relu activation functions in deep neural network. in Intelligent Systems: Proceedings of SCIS 2021, Springer, pp. 39–52.
- Wu, Q., Wang, J., Cao, J., Lu, C., Yang, G., Shi, X., Chuai, X., Gong, Y., Su, Y., Zhao, Y., 2018. Photoelectric plasticity in oxide thin film transistors with tunable synaptic functions. Adv. Electron. Mater. 4, 1800556.
- Wu, D., Yang, X., Wang, N., Lu, L., Chen, J., Zhou, L., Rahman, B.M.A., 2022. Resonant multilevel optical switching with phase change material GST. Nanophotonics 11, 3437–3446.
- Xiang, S., Han, Y., Song, Z., Guo, X., Zhang, Y., Ren, Z., Wang, S., Ma, Y., Zou, W., Ma, B., 2021. A review: Photonics devices, architectures, and algorithms for optical neural computing. J. Semicond. 42, 23105.
- Xie, X., Pu, Y.-F., Wang, J., 2023. A fractional gradient descent algorithm robust to the initial weights of multilayer perceptron. Neural Networks 158, 154–170.
- Xu, R., Lv, P., Xu, F., Shi, Y., 2021. A survey of approaches for implementing optical neural networks. Opt. Laser Technol. 136, 106787.
- Xu, M., Mai, X., Lin, J., Zhang, W., Li, Y., He, Y., Tong, H., Hou, X., Zhou, P., Miao, X., 2020. Recent advances on neuromorphic devices based on chalcogenide phase-change materials. Adv. Funct. Mater. 30, 2003419.
- Yadav, A., Yadav, N., Agrawal, V., Polyutov, S.P., Tsipotan, A.S., Karpov, S.V., Slabko, V. V., Yadav, V.S., Wu, Y., Zheng, H., 2021. State-of-art plasmonic photonic crystals based on self-assembled nanostructures. J. Mater. Chem. C 9, 3368–3383.
- Yamasue, E., Susa, M., Fukuyama, H., Nagata, K., 2002. Thermal conductivities of silicon and germanium in solid and liquid states measured by non-stationary hot wire method with silica coated probe. J. Cryst. Growth 234, 121–131.
- Yang, Y., He, Y., Nie, S., Shi, Y., Wan, Q., 2018. Light stimulated IGZO-based electric-double-layer transistors for photoelectric neuromorphic devices. IEEE Electron Device Lett. 39, 897–900.
- Yang, R., Wang, Y., Li, S., Hu, D., Chen, Q., Zhuge, F., Ye, Z., Pi, X., Lu, J., 2024. All-optically controlled artificial synapse based on full oxides for low-power visible neural network computing. Adv. Funct. Mater. 34, 2312444.
 Yin, L., Han, C., Zhang, Q., Ni, Z., Zhao, S., Wang, K., Li, D., Xu, M., Wu, H., Pi, X., 2019.
- Yin, L., Han, C., Zhang, Q., Ni, Z., Zhao, S., Wang, K., Li, D., Xu, M., Wu, H., Pi, X., 2019. Synaptic silicon-nanocrystal phototransistors for neuromorphic computing. Nano Energy 63, 103859.
- Zhang, Y., Chou, J.B., Li, J., Li, H., Du, Q., Yadav, A., Zhou, S., Shalaginov, M.Y., Fang, Z., Zhong, H., et al., 2019. Broadband transparent optical phase change materials for high-performance nonvolatile photonics. Nat. Commun. 10, 4279.
- Zhang, J., Dai, S., Zhao, Y., Zhang, J., Huang, J., 2020. Recent progress in photonic synapses for neuromorphic systems. Adv. Intell. Syst. 2, 1900136.
- Zhang, T., Fan, C., Hu, L., Zhuge, F., Pan, X., Ye, Z., 2024. A reconfigurable all-optical-controlled synaptic device for neuromorphic computing applications. ACS Nano
- Zhang, H., Huang, B., Zhang, Z., Cheng, C., Zhang, Z., Zhang, H., Chen, R., Chen, H., 2021. On-chip photonic synapses based on slot-ridge waveguides with PCMs for inmemory computing. IEEE Photonics J. 13, 1–13.
- Zhang, H., Huang, B., Zhang, Z., Cheng, C., Zhang, Z., Chen, R., Bao, L., Xie, Y., 2024.
 Multilevel weight optimization of photonic synapses based on slot-ridge waveguides with multi-block GST. Opt. Commun. 550, 130017.
- Zhang, D., Tan, Z., 2022. A review of optical neural networks. Appl. Sci. 12, 5338.
- Zhang, Y., Yao, D., Liu, Y., Fang, C., Wang, S., Wang, G., Huang, Y., Yu, X., Han, G., Hao, Y., 2021. All-optical synapse with directional coupler structure based on phase change material. IEEE Photonics J. 13, 1–6.
- Zheng, J., Khanolkar, A., Xu, P., Colburn, S., Deshmukh, S., Myers, J., Frantz, J., Pop, E., Hendrickson, J., Doylend, J., 2018. GST-on-silicon hybrid nanophotonic integrated circuits: A non-volatile quasi-continuously reprogrammable platform. Opt. Mater. Express 8, 1551–1561.
- Zhou, X., Hu, F., Hou, Q., Hu, J., Wang, Y., Chen, X., 2024. All-photonic artificial synapses based on photochromic perovskites for noncontact neuromorphic visual perception. Commun. Mater. 5, 116.
- Zhu, W., Zheng, G., Cao, S., He, H., 2018. Thermal conductivity of amorphous SiO2 thin film: A molecular dynamics study. Sci. Rep. 8, 1–9.
- Zhuge, X., Wang, J., Zhuge, F., 2019. Photonic synapses for ultrahigh-speed neuromorphic computing. Phys. status solidi (RRL)–Rapid Res Lett. 13, 1900082.
- Zou, X., Zheng, G., Chen, Y., Xian, F., Xu, L., 2019. Actively tunable mid-infrared Fano resonance in Ge2Sb2Te5-based grating structures. Opt. Mater. (Amst) 88, 54–59.